Posted on 5 Oct 2023 — The copyright holder is the author/funder. All rights reserved. No reuse without permission. — https://doi.org/10.22541/essoar.169651354.42556413/v1 — This a preprint and has not been peer reviewed. Data may be preliminary.

Sensitivity of GNSS-Derived Estimates of Terrestrial Water Storage to Assumed Earth Structure

Matthew Jacob Swarr[1], Hilary Rose Martens[1], and Yuning Fu[2]

[1]University of Montana
[2]Bowling Green State University

October 5, 2023

Abstract

Geodetic methods can monitor changes in terrestrial water storage (TWS) across large regions in near real-time. Here, we investigate the effect of assumed Earth structure on TWS estimates derived from Global Navigation Satellite System (GNSS) displacement time series. Through a series of synthetic tests, we systematically explore how the spatial wavelength of water load affects the error of TWS estimates. Large loads (e.g., >1000 km) are well recovered regardless of the assumed Earth model. For small loads (e.g., <10 km), however, errors can exceed 75% when an incorrect model for the Earth is chosen. As a case study, we consider the sensitivity of seasonal TWS estimates within mountainous watersheds of the western U.S., finding estimates that differ by over 13% for a collection of common global and regional structural models. Errors in the recovered water load generally scale with the total weight of the load; thus, long-term changes in storage can produce significant uplift (subsidence) enhancing errors. We demonstrate that regions experiencing systematic and large-scale variations in water storage, such as the Greenland ice sheet, exhibit significant differences in predicted displacement (over 20 mm) depending on the choice of Earth model. Since the discrepancies exceed GNSS observational precision, an appropriate Earth model must be adopted when inverting GNSS observations for mass changes in these regions. Furthermore, regions with large-scale mass changes that can be quantified using independent data (e.g., altimetry, gravity) present opportunities to use geodetic observations to refine structural deficiencies of seismologically derived models for the Earth's interior structure.

Sensitivity of GNSS-Derived Estimates of Terrestrial Water Storage to Assumed Earth Structure

Matthew J. Swarr[1], Hilary R. Martens[1], and Yuning Fu[2]

[1]Department of Geosciences, University of Montana, Missoula, MT, USA
[2]School of Earth, Environment, and Society, Bowling Green State University, Bowling Green, OH, USA

Key Points:

- Estimates of water storage made at fine spatial scales are highly sensitive to the Earth model used to invert geodetic measurements
- Sensitivities to Earth structure produce uncertainties in estimates of water storage that scale with the total weight of the water load
- Predictions of uplift produced by melting of the Earth's ice sheets over the past two decades can differ by over 20 mm between Earth models

Corresponding author: M. J. Swarr, `matthew.swarr@umontana.edu`

Abstract

Geodetic methods can monitor changes in terrestrial water storage (TWS) across large regions in near real-time. Here, we investigate the effect of assumed Earth structure on TWS estimates derived from Global Navigation Satellite System (GNSS) displacement time series. Through a series of synthetic tests, we systematically explore how the spatial wavelength of water load affects the error of TWS estimates. Large loads (e.g., >1000 km) are well recovered regardless of the assumed Earth model. For small loads (e.g., <10 km), however, errors can exceed 75% when an incorrect model for the Earth is chosen. As a case study, we consider the sensitivity of seasonal TWS estimates within mountainous watersheds of the western U.S., finding estimates that differ by over 13% for a collection of common global and regional structural models. Errors in the recovered water load generally scale with the total weight of the load; thus, long-term changes in storage can produce significant uplift (subsidence), enhancing errors. We demonstrate that regions experiencing systematic and large-scale variations in water storage, such as the Greenland ice sheet, exhibit significant differences in predicted displacement (over 20 mm) depending on the choice of Earth model. Since the discrepancies exceed GNSS observational precision, an appropriate Earth model must be adopted when inverting GNSS observations for mass changes in these regions. Furthermore, regions with large-scale mass changes that can be quantified using independent data (e.g., altimetry, gravity) present opportunities to use geodetic observations to refine structural deficiencies of seismologically derived models for the Earth's interior structure.

Plain Language Summary

In many regions of the Earth, water resources used for agriculture, domestic, and industrial purposes rely on stream flow and groundwater sourced from the melting of winter snowpack in adjacent mountains. Modern shifts in climate have resulted in increasingly variable precipitation patterns and temperatures during winter months, coupled with a rising global population, there has been a growing need for accurate estimates of freshwater stored above and beneath the land surface. A relatively new interdisciplinary approach called hydrogeodesy allows for freshwater resources to be accurately monitored by using satellite- and ground-based sensors to accurately measure changes in the shape and gravitational field of the Earth produced by the redistribution of water between natural reservoirs. As this approach becomes increasingly utilized to inform decision-makers, however, we require a deeper understanding of the assumptions and uncertainties of the models used to translate between geodetic measurements and estimates of water storage. Here, we consider the impact of assumptions about the Earth's interior structure on the error of geodetic water storage estimates. We present a set of case studies that display the varied influence of assumed Earth structure on water storage estimates depending on the spatial scale and amplitude of water storage variations.

1 Introduction

Accurate estimates of terrestrial water storage (TWS), defined as the sum of all storage within surface and subsurface reservoirs, are vital in the assessment and effective long-term management of water resources. In addition, accurate assessment of TWS aids in our understanding of the Earth's water cycle and interactions between individual hydrological reservoirs, such as snowpack and groundwater (e.g. Lettenmaier & Famiglietti, 2006; Enzminger et al., 2019). Recent developments in space geodesy, such as the Global Navigation Satellite Systems (GNSS), have become increasingly important in the study of freshwater resources as accurate measurement of subtle changes in the shape and gravitational field of the Earth produced by the redistribution of mass within surface and subsurface hydrologic reservoirs allow for spatially distributed estimates of TWS to be made at local and regional scales (e.g. Wahr et al., 2004; Argus et al., 2014; Milliner et al., 2018; Argus et al., 2022) complimenting other datasets currently used in the assessment and management of water resources.

Most geodetic investigations of TWS, however, have not considered the impact of the choice of Earth structure model on water storage estimates, which may lead to inaccuracies in estimated TWS and misinformed decision making by water managers and policy makers. The deformation response of the Earth due to variations in TWS is controlled by the spatiotemporal characteristics of the hydrologic surface mass as well as the material properties of the Earth's interior. To translate between observations of surface displacement and changes in storage within natural reservoirs, prior knowledge of the Earth's elastic and density structure is required to accurately predict displacement of the Earth's surface to an applied load (e.g. Farrell, 1972; Martens et al., 2019). A majority of studies using GNSS observations to estimate TWS have used globally averaged estimates of Earth structure, such as PREM (Dziewonski & Anderson, 1981) or Gutenberg-Bullen (Alterman et al., 1961), to map between observations of surface displacement and estimates of TWS (e.g Argus et al., 2014; Borsa et al., 2014; Argus et al., 2017; Enzminger et al., 2018).

Recent studies suggest that displacements produced by changes in surface mass can be highly sensitive to the local material properties and structural features of the crust and upper mantle, especially for surface loading occurring at relatively fine spatial scales (e.g.<2500 km^2) (e.g Martens, Simons, et al., 2016; Dill et al., 2015). For example, Martens, Rivera, et al. (2016) computed sensitivity kernels for the load Love number (LLNs) and load Green's function (LGFs), which describe the deformation response of the Earth to an applied unit point load, by systematically perturbing the elastic and density structure of PREM through the crust and upper mantle, finding the LGFs to be predominately sensitive to variations in elastic material properties in the upper 500 km of the Earth. Further, Dill et al. (2015) quantified the effect of sensitivities to local crustal structure on the deformation response to surface loading using grids of local LGFs, finding magnitudes of differences up to 25% for vertical displacement and 91% for horizontal displacement. Such sensitivities offer the possibility of tomographic studies to refine seismologically derived Earth models' structural deficiencies when the loading source is reasonably constrained, such as the Earth's ocean tides (e.g. Ito & Simons, 2011). In the interest of using GNSS observations to better manage water resources across various spatial scales (e.g., continental-scale vs. watershed-scale), assumptions about the Earth's interior structure may significantly bias TWS estimates depending on the spatial scale of interest due to sensitivities to the shallow material properties of the Earth, which can differ significantly across regions.

The uncertainty of TWS estimates associated with choice of Earth structure has only recently begun to be explored. For example, Wang et al. (2015) estimated the effect of assumed Earth structure on estimates of TWS derived from synthetic displacement and gravity observations for the Tibetan Plateau. Utilizing a one-dimensional Earth model that reflected the regional crustal structure of the Tibetan Plateau, they produced forward modeled surface displacements from an input hydrologic load model. Following this, an inversion of the synthetic displacements revealed that only 88% of the input load could be recovered when using an *a priori* Earth model that differed from the one-dimensional local crustal structure of the Tibetan Plateau. However, the study was limited to a single load size that spanned the area of the Tibetan Plateau ($\sim$ 2.5 million km^2).

Here, we investigate the sensitivity of surface loading to assumed Earth structure to assess the associated implications in using geodetic measurements to estimate changes in storage within natural reservoirs. We quantify the sensitivity of GNSS-inferred TWS estimates to assumed Earth structure through a series of synthetic tests where displacements produced by surface loads with varying spatial wavelength are inverted while assuming a suite of different reference Earth models. We then present a case study for the western U.S., where we examine nearly two decades of seasonal TWS estimates produced from a variety of global and regional Earth models. Finally, we consider the impact of assumed Earth structure on predicted surface displacement in regions experiencing long-term (i.e., interannual to decadal) changes in mass within surface and subsurface reservoirs and identify regions where GNSS-inferred estimates of hydrologic and cryospheric loading may be significantly biased unless an appropriate model for the interior structure of the Earth's is adopted.

2 Synthetic Tests

To quantify the sensitivity of GNSS-inferred TWS estimates to assumed Earth structure, we carry out a series of synthetic tests which closely reflect the process and underlying logic applied when using real GNSS data to estimate changes in TWS. We create a set of synthetic surface displacements for a single spherically symmetric, non-rotataing, elastic, and isotropic (SNREI) Earth model, which we take to the be unknown *true* structure of the Earth. We then invert the synthetic displacements for estimates of TWS, while assuming another SNREI Earth model in the design matrix of our inversion. By simulating scenarios where the assumed model for Earth structure differs from the *true* structure, we can the quantify the error in TWS estimates associated with the choice of an *a priori* SNREI Earth model used in the inversion. Furthermore, by systematically varying the spatial wavelength of the loads used here, we assess the scale dependencies of the errors. Here, we focus on the sensitivities of TWS estimates to choice of radially symmetric Earth model. To gain insight into how lateral contrasts in elasticity and density affect the estimates of TWS, we include both global- and regional-scale models in our comparisons.

2.1 Earth Models

To provide a broad sample of structural models for the Earth's interior, we consider common reference Earth models: PREM (Dziewonski & Anderson, 1981), AK135f (Kennett et al., 1995; Montagner & Kennett, 1996), STW105 (Kustowski et al., 2008), and 1066A (Gilbert & Dziewonski, 1975), which represent globally averaged estimates of Earth structure (Fig. 1). Additionally, we consider regional Earth models: CR (Chu et al., 2012)(Chu et al. 2012) and SNA (Grand & Helmberger, 1984), which represent cratonic and stable North American structures. For SNA and CR, beneath approximately 1000 km depth we assume the material properties of AK135f. Lastly, we consider models derived from LITHO1.0 which reflect local crustal and upper mantle structure on a 1° tessellated global grid (Pasyanos et al., 2014). We consider LITHO1.0 models within the western U.S. as there is a variety of geologic settings within the region (e.g., sedimentary basins, mountain ranges) and later sections of the work presented here are concerned with quantifying the effect of assumed Earth structure on GNSS-inferred TWS estimates within specific mountain provinces of the region.

From LITHO1.0, three local one-dimensional Earth models were constructed to represent the average local crust and upper mantle structure of the San Joaquin, Sacramento, Tulare (SST) River Basin, the Sierra Nevada, and the Cascade Range respectively. For each local model, we consider multiple LITHO1.0 models within the region to produce an estimate of the average local crustal structure. The sampling locations in which the local crustal models were derived from LITHO1.0 as well as the local lithosphere thicknesses, below which we assume the material properties of AK135f, are displayed in Table S1. For models that contain an ocean layer at the surface, we average the material properties of the ocean layer and uppermost crustal layer to form a single homogeneous layer. The density of the top layer is equal to the weighted mean density of the two original layers, which conserves total mass, and the elastic moduli are equal to those of the original uppermost crustal layer (Guo et al., 2004; Martens & Simons, 2020).

Using *LoadDef* (Martens et al., 2019), we compute LLNs, LGFs, design matrices, and forward modeled surface displacements. LLNs were computed from spherical harmonic degree $n = 0$ to $n = 1e5$ to ensure that the Love Numbers of Earth models with relatively fine sedimentary layers in the uppermost crust converged with the asymptotic approximation of the LLNs. LGFs for each model considered in this manuscript are displayed in the supplementary materials of this work (Fig. S1). All synthetic surface displacements are computed assuming the Earth model PREM. Thus, we assume PREM represents the *true* structure of the Earth in the synthetic tests presented here.

2.2 Load Models

We consider Gaussian-shaped surface loads to derive the synthetic surface displacements. The load models represent isotropic bivariate normal distributions with a standard deviation, σ, approximately equal to the Gaussian load's half width at half maximum (HWHM). Each surface load has a maximum height of one meter of freshwater at its center, which smoothly decays towards zero. For distances greater than four HWHM lengths from the center of the load model, we truncate the load model and consider the load amplitude to be equal to zero. We consider input load models of varying size (HWHMs equivalent to 1 km, 2.5 km, ... , 750 km, 1000 km) to explore a variety of hydrologically relevant spatial scales.

For each load model, surface displacements were computed for an evenly spaced grid of synthetic GNSS stations, $(a/8)$ km x $(a/8)$ km resolution, where a is the HWHM of the respective input load model. Synthetic displacements were computed with respect to the center of mass of the solid Earth, commonly referred to as the CE reference frame (Blewitt, 2003). Additionally, we consider the predicted displacements used in these synthetic examples to be noise free, which allows for the sensitivity of TWS estimates to Earth structure alone to be isolated. The input load model, distribution of synthetic GNSS stations, and predicted displacements for a 10 km HWHM load are shown in Figure. 2.

2.3 Inverse Model

For each load model and synthetic station grid, we perform an inversion of the the synthetic vertical displacements to estimate the input surface load. The recovered load height is assumed to be uniform within every grid cell of the inversion grid. We solve for the load within each grid cell by minimizing the damped least squares problem

$$\|(G_i m - d)\|_2^2 + \alpha^2 \|(Lm)\|_2^2 \tag{1}$$

where G_i is the [n x m] design matrix containing the predicted elastic response of assumed Earth structure i at each synthetic GNSS station to 1 meter of freshwater placed in each grid cell of the model grid, m is the [m x 1] vector of unknown quantity of water distributed uniformly within each grid cell, d is the [n x 1] vector of synthetic vertical displacements at each station assuming PREM structure, L is a 2-D finite difference Laplacian operator used to enforce smoothness between neighboring grid cells, and α is a regularization parameter, where higher α values result in smoother variations in estimated surface mass between adjacent grid cells (Aster et al., 2019).

In order to avoid potential model bias induced by edge effects along the boundaries of our model domain as well as through the use of the Laplacian operator, we take two steps to ensure discrepancies in our final estimates of surface load are resultant of the differences in Earth structure between the Earth models used to produce our data vector and design matrix respectively. To avoid bias induced by the Laplacian operator, we construct load-model grids of equal resolution to that of the synthetic station grid, where there is one synthetic GNSS station located at the center of each model grid cell. This

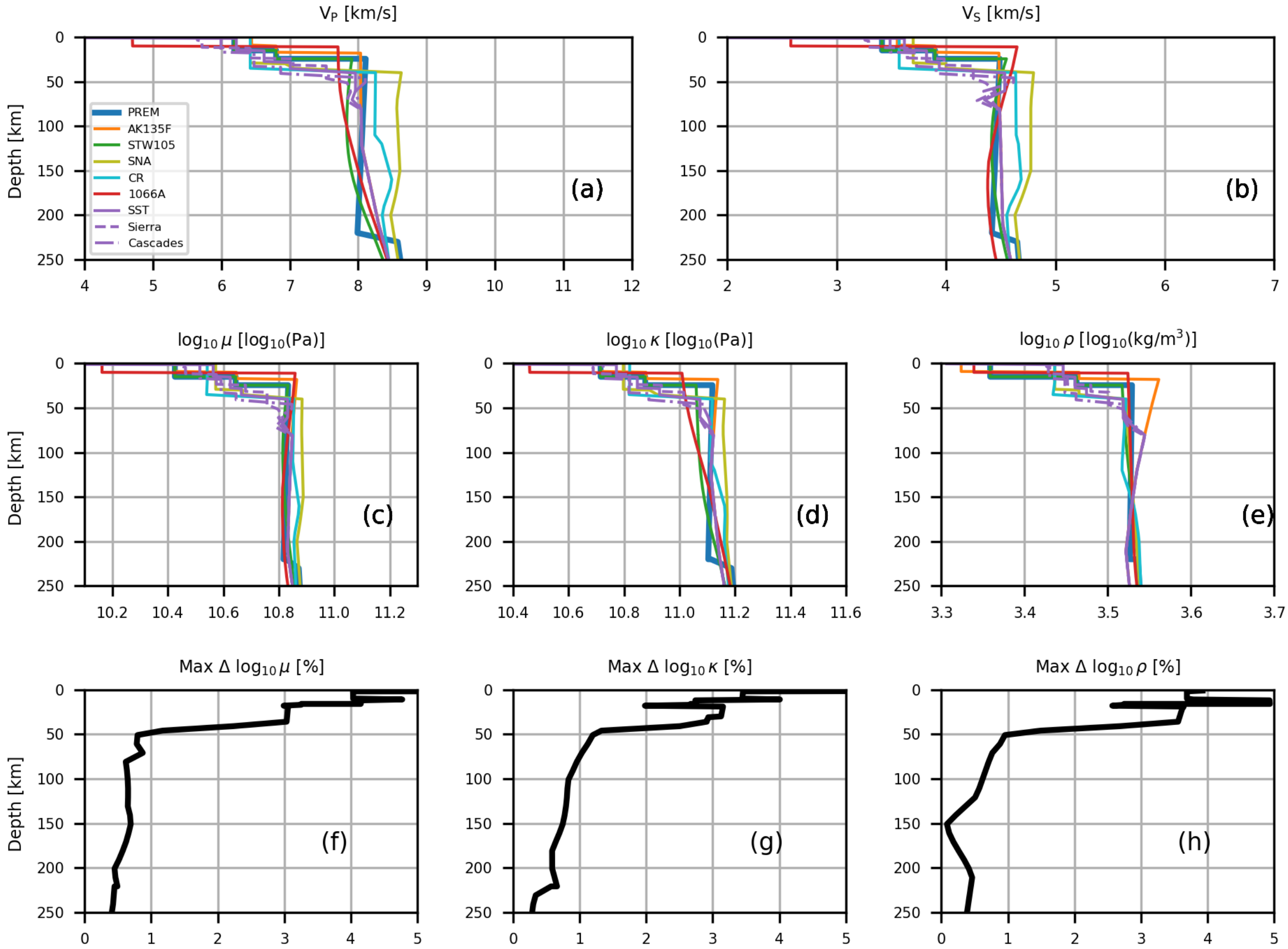

Figure 1. Depth profiles through the middle mantle of one-dimensional Earth models: PREM (blue), AK135f (orange), STW105 (green), SNA (olive), CR (cyan), 1066A (red) as well as models derived from the LITHO1.0 for the San Joaquin, Sacramento, Tulare River Basin (purple) and Sierra Nevada (dashed purple) of California as well as the Cascade Range (dash-dot purple) of Washington, Oregon, and northern California. Panels (a) & (b) show P-wave (V_p) and S-wave (V_s) velocity as a funciton of depth. Panels (c)-(e) show the shear modulus, bulk modulus, and density profiles in log-space. Panels (f)-(h) show the maximum percentage difference between the set of Earth models in log-space as a function of depth for the two elastic parameters and density respectively. Adapted from Martens (2016) (cf. Fig.A1).

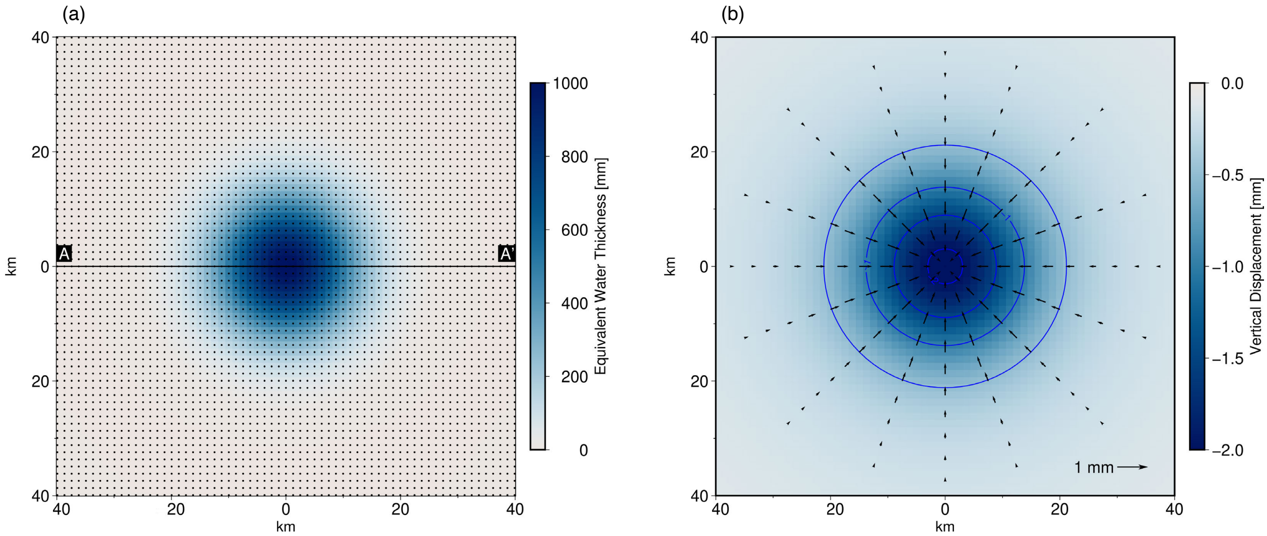

Figure 2. a) 10 km HWHM Gaussian load model used for synthetic loading tests. Black dots represent the location of synthetic GNSS stations used to produce the synthetic vertical displacements assuming the material properties of PREM as well for estimating surface mass loading utilizing a suite of other one-dimensional Earth models described in Section 3.1. The load amplitude, denoted by the left color bar, represents the height of freshwater distributed evenly within each pixel of the input load model. Subsequent figures display estimated surface load and error along the profile line (A - A'). b) Forward modeled vertical and horizontal displacement produced through the convolution of the LGFs of PREM with the load model depicted in a). The magnitude of vertical displacement is denoted by the right color bar. Blue contour lines represent 0.5 mm intervals of vertical displacement. The magnitude and direction of horizontal displacement produced by the load model are depicted as black vector, with a reference vector located in the lower right corner of panel b).

ensures that the number of observations n is equal to the number of model parameters m being solved for, making our linear system even-determined with a unique solution. As a result, eq. (1) reduces to

$$\|(G_i m - d)\|_2^2 \,. \tag{2}$$

To address unwanted edge effects, we alter the original boundary of our model domain to extend 8 half width lengths from the center of each load model. Upon solving eq. (2), we then only consider model grid cells within 4 half width lengths from the center of the load model for further analysis. Similar to previous studies, we find estimates of surface load to be sensitive to the location of the model domain's boundaries (e.g. Fu et al., 2015). When the edge of the model domain is not extended from its original position, we observe the value of estimated surface load within grid cells along the edge of the domain to be nearly 30% greater than the true value represented by the input load model.

To quantify the sensitivity of GNSS-inferred TWS estimates to assumed Earth structure, we compute the error, $m_i - m_{true}$, between the estimated surface load produced assuming Earth structure i and the *true* load model used to produce the synthetic displacements used in eq. (2). We display estimates of surface load derived from the suite of Earth models considered here as well as their error relative to the true load's value along a profile, which crosses the center of each load model (A-A') (Fig. 2).

2.4 Effect of Assumed Earth Structure on Estimated Surface Loading

Estimated surface load and error profiles for select load models are displayed in Figure. 3. Relative error between estimates of surface load and the *true* load model are maximized at relatively fine loading scales (e.g., <10 km HWHM), where the *true* load's value can be incorrectly estimated by over 75% at the center of the load for select Earth models (Fig. 3, Fig. 4). Similarly, we find for loads with relatively small spatial wavelengths, errors in the recovered load can span the entire area of the load model (e.g., Fig. 3b). In comparison, as the spatial wavelength of the surface load becomes progressively large, error in recovered load is primarily concentrated within one half width length from the center of the load and is near zero for distances beyond this (e.g., Fig. 3h).

As the Earth's response to surface loading occurring at relatively fine spatial scales is predominately controlled by the shallow material properties of the Earth (Martens, Rivera, et al., 2016), discrepancies in estimated surface load reported here reflect differences in the Earth model used to construct the design matrices of our inverse problem, which may contain multiple sedimentary layers in the uppermost crust or a deep cratonic keel, and the globally averaged estimate of Earth structure used to produce the data vector. Such discrepancies are most apparent for Earth models that represent regional estimates of structure, such as CR and SNA, or those representing local crustal structure of specific regions within the western U.S., which differ significantly from the upper crustal structure of PREM (Fig. 1). Additional surface load and error profiles for surface loads characterized by other spatial wavelengths considered as a part of this work are provided in the supporting information (Fig. S2-S5).

We therefore find that an incorrect assumption about the material properties of the Earth may yield highly incorrect estimates of surface load when estimating changes in storage within natural reservoirs occurring over short distances, and that errors associated with assumed Earth structure diminish as the spatial wavelength of loading becomes increasingly large (Fig. 4a). Errors tend to be less than 10% of the *true* load's value when considering surface loads with a HWHM greater than 10 km and become even smaller, less than 2%, as the load HWHM approaches 1000 km. Such findings are consistent with an increasing sensitivity to Earth structure over broader depth ranges as the size of sur-

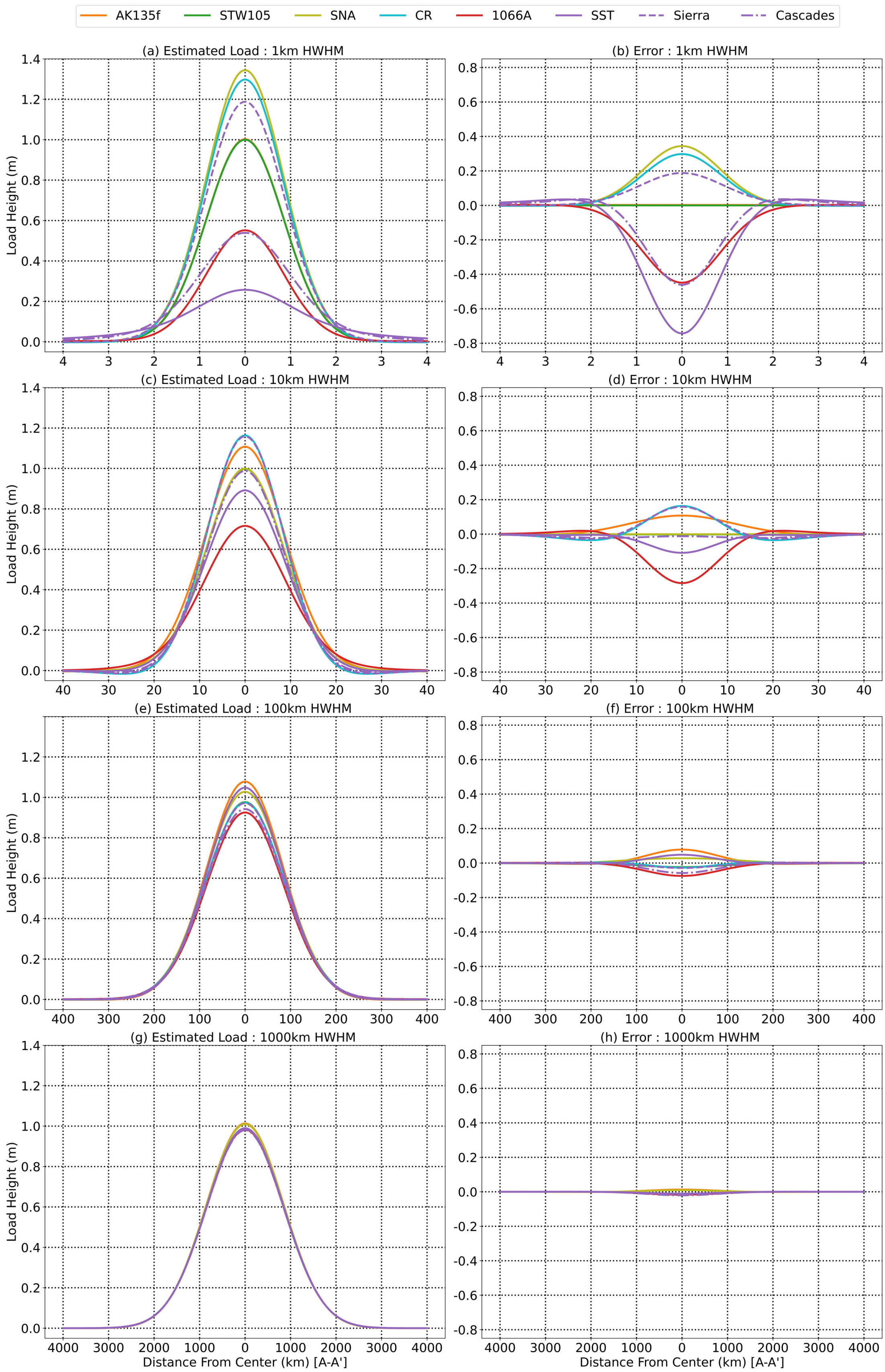

Figure 3. Estimated surface load and associated error for inversion estimates assuming the SNREI Earth structures shown in Fig. 1 along the profile A-A' in Fig. 2 for surface loads corresponding to HWHMs of: (a-b) 1 km, (c-d) 10 km, (e-f) 100 km, and (g-h) 1000 km.

face loading increases (Martens, Rivera, et al., 2016), which reduces the sensitivity to highly variable shallow Earth structure (Fig. 1). Errors for Earth models that differ from PREM over broad depth ranges, however, such as STW105 and AK135f, become increasingly large relative to the error for other models that deviate from PREM primarily in the crust and upper mantle (Fig. S2-S5).

As expected, the differences between the estimated and true load's values can be related to the differences in LGFs between the SNREI Earth models used to generate the data vector, d, and the design matrix, G, of the inverse problem. For instance, the LGFs for SNA exhibit smaller displacements within the range of $0.001^\circ - 0.1^\circ$ relative to PREM, which would correspond to lower amplitude displacements relative to PREM for distributed loads within this range (Fig. S1). When inverting the synthetic displacements that reflect PREM's response to the input load, a design matrix corresponding to SNA overestimates of the true load's value (e.g., Fig. 3a). This is the result of SNA producing smaller amplitude displacements relative to PREM when an identical load is applied to both. If the data vector, d, consists of displacements derived from a 'soft' Earth model (in this case, PREM) relative to a 'hard' Earth model described by the design matrix, G, there will be a systematic overestimation of the true load's value. Similar relationships are found for Earth models with LGFs that exhibit displacement amplitudes greater than those of PREM, such as 1066A – the true load's value will be systematically underestimated.

In addition to increased sensitivity to Earth structure for relatively small surface loads, we find sensitivities generally follow the geometry of the Gaussian load model used to produce synthetic displacements, where the largest errors in estimated surface load are located near the center (and peak) of the load model (Fig. 4b). For example, we find that error in recovered water load decreases by a factor of two within one half width length of the center of the load. Similarly, for distances greater than two half width lengths, errors tend to be less than 5% of the load model's true value, irrespective of the load model's spatial wavelength. Such findings are consistent with previous studies that have found differences in predictions of surface loading between Earth models are maximized in areas where the amplitude of surface loading is relatively large or at small observer-to-load distances (e.g. Ito & Simons, 2011; Martens, Simons, et al., 2016; Argus et al., 2017). Our findings highlight the potential impact of an incorrect assumption about the Earth's interior structure on GNSS-inferred estimates of TWS made across broad regions. For instance, when estimating variations in storage within the region surrounding the Sierra Nevada of California (e.g. Enzminger et al., 2018), sensitivities to Earth structure will yield errors in estimated TWS concentrated within the mountains, where surface loading is particularly large as a result of the seasonal accumulation of rain and snow, with errors quickly decaying in adjacent regions where the amplitude of surface loading is small relative to the nearby mountains.

While this appears to be generally true, we find for particular Earth model-load model combinations, peak sensitivity can be shifted away from the center of the load (Fig. S6-S8). We believe these increased sensitivities away from the center of the load model to be resultant of differences in the elastic and density structure of a chosen Earth model with that of PREM over a specific depth range. For example, an inversion assuming the structure of CR exhibits peak sensitivity for a 25 km HWHM load at a distance of 30 km from the center of the load model. When comparing the elastic and density structure of PREM and CR, we find there to be a $\sim$2.7% reduction in the elastic and density parameters of CR relative to PREM between depths of 24-40 km. Similar results were found in Martens, Rivera, et al. (2016) where ocean tidal loading sensitivities shifted inland away from the coast, where displacements were maximized, as the elastic and density structure of PREM was systematically perturbed over various depth ranges.

In absolute terms, the results here display the impact of an incorrect assumption about the Earth's interior structure when using geodetic observations of surface load-

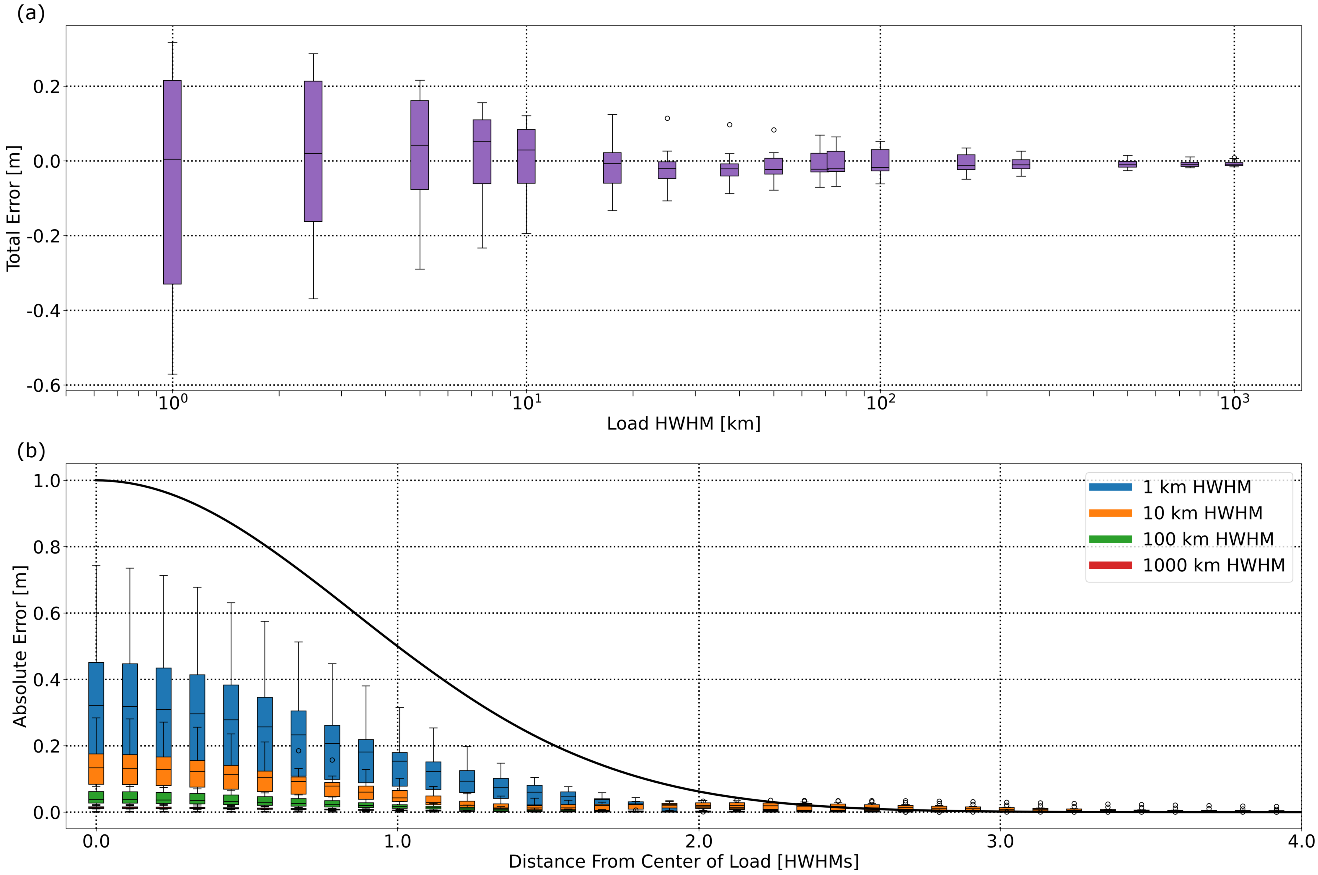

Figure 4. (a) Distribution of total error between estimates of surface load derived from the eight Earth models considered here and the *true* load model as a function of load HWHM size. Load HWHM along the x-axis is displayed on a logarithmic scale. (b) Distribution of absolute error for the Earth models considered here as function of distance from the center of the load model for load models used in Fig. 3. As the load models used here only vary in size, but retain their geometry, distances on the x-axis are plotted as half width lengths away from the center of the load model. The black line represents the profile of the input Gaussian load-model used to produce synthetic displacements.

ing across spatial scales relevant for the effective management of freshwater resources. For example, an incorrect assumption about the Earth's local crustal properties may yield errors nearly as large as 0.8 m when considering a one meter surface load spanning a few kilometers. Consequently, the synthetic tests presented here shed light on the uncertainties that arise from using observations of hydrology-induced surface loading to estimate TWS. Hydrogeodesists and water managers must be aware of the biases that can be introduced through assumptions about Earth structure in the modeling process, since uncertainties in estimated TWS can be significant, especially at small spatial scales.

3 Western U.S. Case Study

To build from the synthetic tests, we consider a case study for the western U.S. that explores the impact of Earth structure on inversions for TWS that use real geodetic data. When working with real data, we do not know the true structure of the Earth, yet we must still select an Earth model to construct the design matrix of the inverse problem. Furthermore, hydrologic loads can exhibit highly heterogeneous spatial patterns across a range of spatial and temporal scales (Skøien et al., 2003). Additionally, the distribution of GNSS stations used to estimate variations in TWS are non-uniformly distributed, which can affect the ability to resolve variations in TWS occurring at relatively fine spatial scales.

To further assess the effect of assumed Earth structure on TWS estimates derived from observations of surface loading and quantify the associated uncertainty using real data, we consider seasonal variations in TWS in the western U.S. between January 1, 2006, and September 30, 2022. We selected the western U.S. as an illustrative and relevant example as (1) the region contains a dense network of GNSS stations allowing for estimates of TWS to be made at a relatively fine spatial scale (approx. 25 km); (2) many stations in the region have long and continuous periods of record, allowing for variations in TWS associated with prolonged periods of drought and precipitation to be made; and (3) the application of space geodetic observations to estimate changes in TWS within the region has been a topic of increasing interest over the past decade in light of several cycles of major drought and recovery (e.g. Argus et al., 2014; Borsa et al., 2014; Carlson et al., 2022; Argus et al., 2022).

3.1 Isolating Seasonal Hydrologic Loading

For this case study, we consider vertical displacements observed within the western U.S. (defined as $31.75°N - 50.25°N, 124.75°W - 103.25°W$) associated with seasonal fluctuations of storage within hydrologic reservoirs. We initially obtain 2961 daily vertical GNSS station time series estimated by the Nevada Geodetic Laboratory (NGL) in the IGS14 reference frame (Blewitt et al., 2018; Kreemer et al., 2018).

To isolate the effect of seasonal changes in TWS on station positions, we carried out the following post-processing steps: (1) identify and discard stations with less than 5 years of data during our period of study (January 2006 to September 2022); (2) remove predicted vertical displacement associated with nontidal atmospheric and nontidal oceanic loading using daily averaged estimates from the German Research Center for Geosciences Postdam (GFZ) (Dill & Dobslaw, 2013); (3) estimate and remove vertical displacement associated with glacial isostatic adjustment (GIA) using estimates from ICE-6GD (VM5a) (Peltier et al., 2018); (4) remove segments of data shorter than 60 days and separated by other data by at least 60 days, as these isolated segments may reflect station-specific equipment malfunctions; (5) remove time series offsets larger than 8 mm associated with known earthquakes and equipment changes using a catalog of known events and offset amplitudes provides by the GAGE facility (Herring et al., 2016); (6) for coseismic offsets larger than 40 mm, fit and remove a logarithmic decay model to characterize post seismic relaxation (Kreemer et al., 2006); (7) remove outliers using a median absolution deviation (MAD) filter with a running median window of 30 days and a median absolute deviation threshold factor of 10; (8) fit and remove the linear trend from each time series to remove secular signals such as uplift associated with periods of drought from the station positions; (9) convert daily position estimates into mean monthly estimates; (10) remove elastic deformation produced by variations in TWS occurring outside of the western U.S. by forward modeling displacements inferred from the Jet Propulsion Laboratory's monthly GRACE mascon solution (version RL06.1M) (Landerer et al., 2020; Watkins et al., 2015; Wiese et al., 2016) using the Earth model PREM; and (11) estimate and remove each year's mean vertical position to remove displacements associated with interannual variations in TWS (i.e., interannual drought and wet periods). We follow the procedure described in Argus et al. (2022) for interpolating GRACE estimates of TWS to periods in which GRACE or GRACE-FO estimates are unavailable.

Following these steps, we identify stations that exhibit peak vertical uplift during the winter months to be exhibiting poroelastic behavior associated with the filling of local aquifers. We identify and remove 134 stations exhibiting poroelastic behavior. Additionally, we identify and remove 30 stations dominated by volcanic deformation primarily near the boundaries of the Long Valley Caldera and the Yellowstone hotspot. Finally, we remove 16 stations predominately located near the epicenters of the Baja and Ridgecrest earthquakes that have been strongly biased by postseismic transients. Following these steps and subsequent removals, we are left with seasonal changes in vertical position for 1685 stations within the study region. As the time series for some stations are not continuous throughout the duration of this study, each time step in the inversion contains a varied number of observations in the data vector. The final list of stations chosen to be used in this study can be found in the supplemental materials (Data Set S1).

3.2 Estimating Seasonal Variations in TWS from Observed Vertical Displacement

We performed an inversion of the observed monthly averaged elastic vertical displacements to estimate monthly changes in seasonal TWS in the western U.S. between January 2006 and September 2022 on a regular model grid with a resolution of 1/4°. Following a similar approach as that described in Section 2., we minimize the damped least squares problem where G_i represents the design matrix associated with assumed SNREI Earth model i. All estimates of TWS reported here are considered anomalies relative to the January 2006 - September 2022 temporal mean.

Due to the uneven distribution of GPS stations in the region, particularly along the eastern portion of our study area, we find there can be large mass anomalies we deem nonphysical (Fig. S9). We believe these features to be the result of a lack of observational constraints in these regions, as well as geophysical signals that were not removed or improperly removed during the post-processing steps described in Section 4.1. To prevent such features from biasing our estimates of TWS, we incorporate additional constrains on the size of the model, equivalent to applying zeroth-order Tikhonov regularization (Aster et al., 2019). Thus, to estimate changes in TWS in the western U.S., we augment eq. (1) as follows

$$\|(G_i m - d)\|_2^2 + \alpha^2 \|(Lm)\|_2^2 + \beta^2 \|(m)\|_2^2 \tag{3}$$

where β is the added regularization parameter that controls the relative amplitude of the model parameters. Like many inverse problems, the problem is ill-posed and underdetermined, thus the problem is non-unique. The regularization parameters α and β act to limit the number of solutions, m, that can adequately fit the data vector, d. We use the L-curve criterion (Hansen, 1992), to determine optimal values of α and β that minimize the residual between the best-fit model and data vector while keeping solutions smooth and parameter amplitudes relatively small. Through L-curve analysis, we find the optimal values of α and β to be 2.5 and 1.0 respectively.

3.3 Sensitivity of Estimated Seasonal Hydrologic Loading to SNREI Earth Structure

We now compare monthly TWS estimates derived from the suite of Earth models introduced in Section 3.1. For this case study, we omit two Earth models (SNA and CR) that reflect continental shield and cratonic structure respectively as they would improperly describe the material properties and structural features of the western U.S. To develop a general understanding of the sensitivity of seasonal TWS estimates in the western U.S., for each Earth model used here we compute monthly stacked estimates of TWS throughout the study period. It should be noted that while monthly stacked estimates of storage allow us to consider the sensitivity of TWS estimates to Earth structure during a 'typical' seasonal fluctuation in storage within the region, there can be considerable interannual variation in seasonal amplitude of TWS associated with years of higher/lower than average winter precipitation (e.g Enzminger et al., 2019), which may result in increased/decreased sensitivity to Earth structure owing to variations in seasonal amplitude (Fig. 7a).

Figure 5. depicts the monthly stacked estimate of storage for the month of April assuming PREM and the direct difference between estimates derived from the other Earth models considered here. For the month of April, mountainous regions of the western U.S., such as the Sierra Nevada and Cascade Range are estimated to have high amplitude seasonal changes in storage within surface and subsurface reservoirs as large as 300 mm of equivalent water thickness relative to the mean annual storage. Adjacent regions are estimated to experience declines in storage during the month of April, such as the Willamette Valley of Oregon, or report lower amplitude changes in storage, typically less than 100 mm of equivalent water thickness, for the month of April.

As peaks in storage are estimated to occur primarily within mountainous regions during the month of April, we naturally find the largest discrepancies between estimates derived from different Earth models within these regions (Fig. 5b-g). For example, differences in estimated storage derived from PREM and other Earth models that represent globally averaged estimates of Earth structure, such as AK135f and 1066A, can be as large as 40 mm in equivalent water thickness and extend across broad regions of the western U.S., typically spanning the entire length of mountain ranges, such as the Sierra Nevada (e.g., Fig. 5b). Conversely, regions estimated to have relatively small amplitude changes in seasonal storage exhibit differences that are typically less than 10 mm in amplitude. Discrepancies between estimates derived from PREM and STW105 tend to be on the order of 5 mm or less extending across broad regions of the western U.S. When considering differences between estimates of TWS derived from PREM and LITHO1.0 models constructed to reflect the local Earth structure of specific regions within the western U.S., we find differences as large as 90 mm of equivalent water thickness, but such discrepancies are confined to relatively small areas within the study region, such as the area surrounding Lake Tahoe of California and Nevada (e.g., Fig. 5e).

Figure. 6 depicts the monthly stacked estimate of seasonal storage for the month of October. In contrast to estimates for the month of April when storage is typically at its annual maximum in the western U.S., October is often characterized as the time of the year in which storage is at its annual minimum, as precipitation in the form of rain and snow is negligible in a majority of the western U.S. As such, it is expected that our estimates of seasonal TWS in the western U.S. for the month of October are predominately negative and nearly equal in amplitude to estimates made for the month of April. For example, we find most mountainous areas to exhibit average storage deficits equal

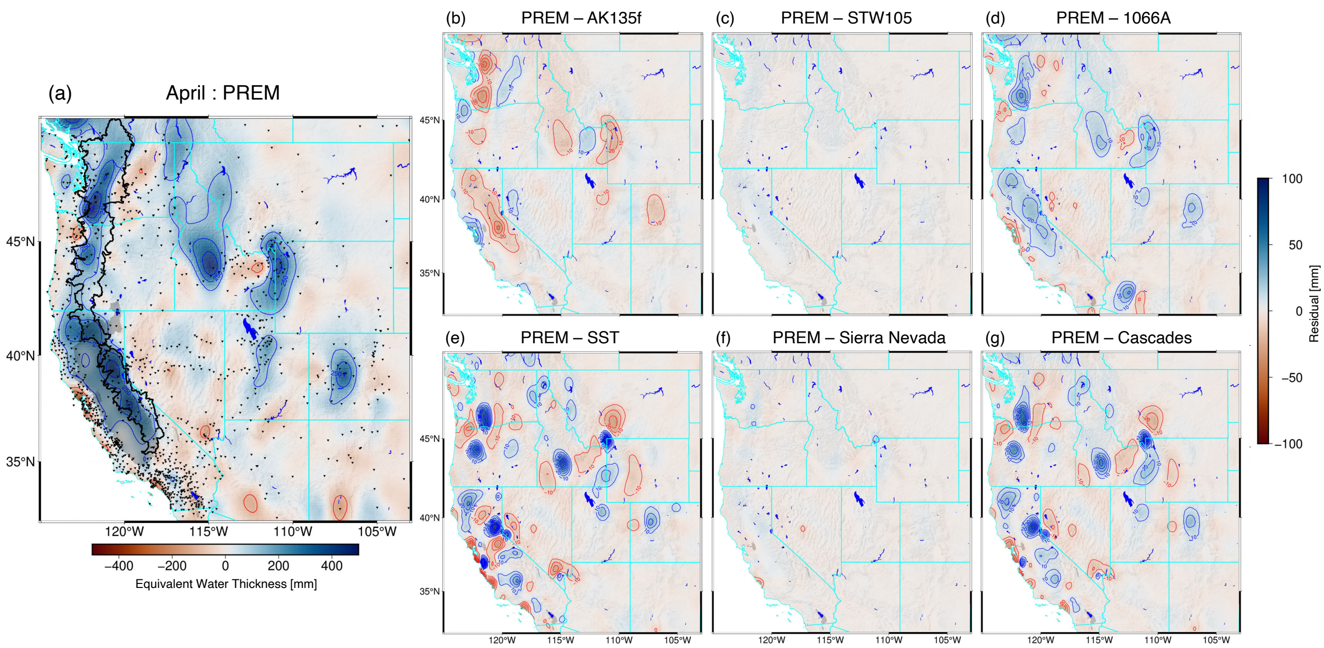

Figure 5. (a) Multi-year monthly stacked estimate of seasonal change in storage for the month of April. Sharp black lines define the boundaries of the HUC-8 watersheds within the Sierra Nevada and Cascade Range respectively. The gray shaded region represents the area constituting the SST River Basin of California. Black inverted triangles represent GNSS stations within the western U.S. used to constrain variations in seasonal TWS. Contours represent 125 mm intervals of equivalent water thickness. Direct differences between pairs of TWS estimates for the month of April using select Earth models: (b) PREM and AK135f, (c) PREM and STW105, (d) PREM and 1066A, (e) PREM and LITHO1.0 model for the SST River Basin, (f) PREM and LITHO1.0 model for the Sierra Nevada, and (g) PREM and LITHO1.0 model for the Cascade Range. The color bars at right denotes the amplitude of the residuals between TWS estimates. Contours represent 10 mm residual intervals of equivalent water thickness.

to 250 mm of equivalent water thickness. Similar to the month of April, when comparing estimates made assuming different models to represent the structure of the Earth, the largest discrepancies are found in regions experiencing the highest amplitude changes in seasonal storage. Discrepancies in estimated TWS between PREM and other globally averaged estimates of Earth structure yield differences as large as 30 mm spanning broad regions that align with major mountain provinces of the western U.S. Estimates of TWS assuming the local LITHO1.0 models can differ from estimates made assuming PREM within relatively small areas by over 80 mm of equivalent water thickness. Estimates of seasonal TWS and direct differences between the Earth models considered here for other months are included in the supplemental materials (Fig. S10-19).

As water storage dynamics in the western U.S. have been found to be closely tied to the annual accumulation and melting of snowpack deposited in mountains during winter months (e.g Brown et al., 2008), we find it reasonable that estimates of seasonal TWS would exhibit the largest sensitivities to Earth structure in mountainous areas where the seasonal accumulation of precipitation is relatively large. In addition, we find the discrepancies displayed in Figs 5-6 between Earth models to reflect differences in the material properties of each Earth model being used here. For example, the local LITHO1.0 models used here may contain multiple sedimentary units in the uppermost crust of the Earth, yielding higher amplitude LGFs in the near-field compared to PREM (Fig. S1). As a result, estimates of TWS derived from the LITHO1.0 models tend to differ from estimates made with PREM at relatively high amplitude over small distances (Figs. 5-6). These differences may reflect GNSS stations observing localized hydrologic loading, such as changes in storage within a nearby lake or artificial reservoir. Although, we note that the estimates derived from the LITHO1.0 model for the Sierra Nevada, which lacks sedimentary units in its uppermost crust, differ from estimates assuming the structure of PREM by less than 10 mm of equivalent water thickness. In contrast, the material properties of the other Earth models being considered tend to differ from PREM over much broader depth ranges, resulting in larger sensitivities to loading occurring within the mid-field. Discrepancies spread across many layers yield relatively smaller amplitude discrepancies in estimates of TWS that span much broader regions of the western U.S.

We now consider the effect of differences in assumed Earth structure on estimates of seasonal TWS within specific mountain and agricultural provinces vital for the effective management of freshwater resources within the western U.S. Figure. 7 displays estimates of seasonal TWS for the SST River Basin, Sierra Nevada of California and the Cascade Range of Washington, Oregon, and northern California derived from the suite of Earth models considered here. Boundaries for each province are depicted as black or shaded regions in Figs 5-6 and are defined by the boundaries of watersheds within each region. We find that estimates of storage can differ by up to 12.4, 13.6, and 9.8 percent of the annual oscillation of storage within each of these regions respectively and are maximized in spring and fall months when storage within natural reservoirs is assumed to be at its annual maximum/minimum.

Of the Earth models considered here, we find AK135f to yield the most discrepant estimates of TWS within the western U.S. When discarded from our analysis, we find estimates of TWS within the SST, Sierra Nevada, and Cascades to vary by 6.7, 7.2, and 5.4 percent respectively. Inspection of the LGFs of AK135f reveal smaller displacements at angular distances between 0.001 and 1.0 degrees compared to the LGFs of the other Earth models considered here (Fig. S1). Such discrepancies between LGFs may be partly explained by AK135f containing a relatively rigid elastic structure in the upper 80 km of the Earth (Fig. 1). Furthermore, such discrepancies may indicate that hydrologic surface loading observed by GNSS stations within the western U.S. is characterized by a spatial wavelength on the order of tens of kilometers, increasing sensitivities to differences in structure between a chosen *a priori* Earth model and the *true* structure of the Earth over these depths (Martens, Rivera, et al., 2016).

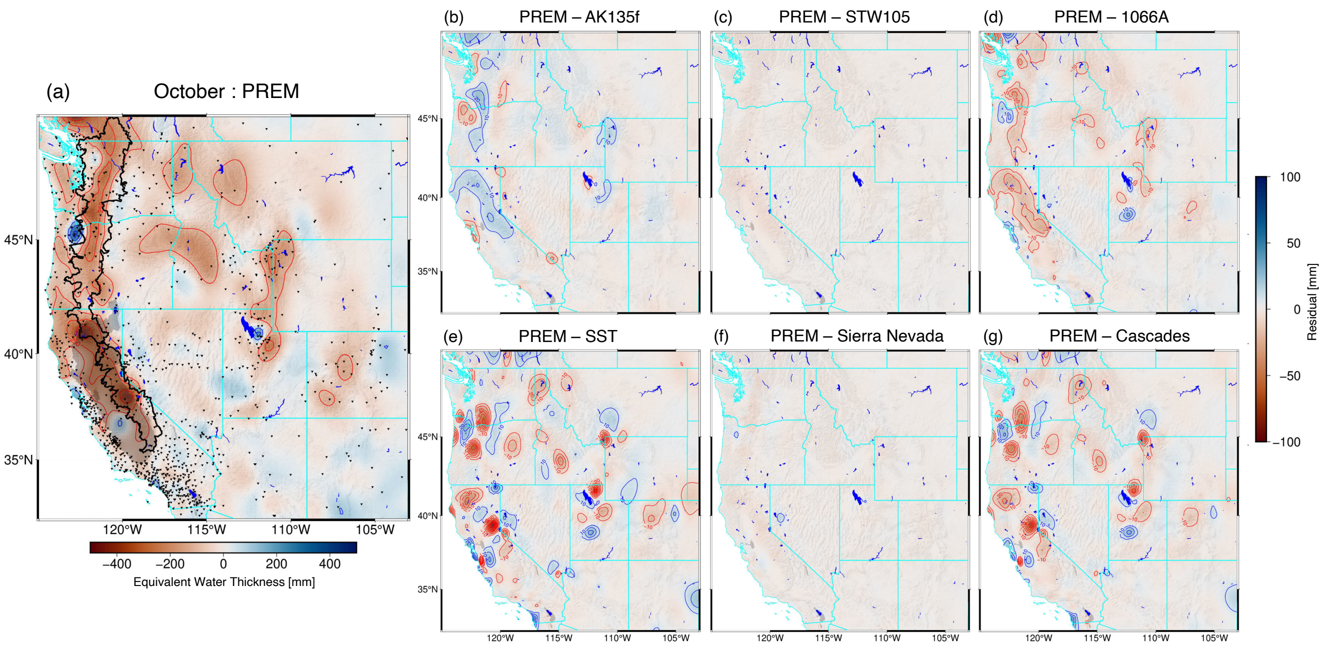

Figure 6. (a) Same as Fig. 5, but for the month of October.

When estimating seasonal changes in storage within individual mountain and agricultural provinces of the western U.S., we find that estimates assuming different models for the interior structure of the Earth differ by less than 14% and differences in estimates of storage remain small relative to reported formal uncertainties of GNSS-inferred TWS estimates within the region (e.g. Argus et al., 2017; Carlson et al., 2022). Nonetheless, water managers and policy makers should be mindful of the uncertainties associated with specific assumptions underlying the models used to convert geodetic measurements into estimates of TWS. Although, we should note that the results presented here only provide a sense of precision of estimated seasonal TWS within the western U.S. The true error in estimated TWS may be much larger if all of the Earth models considered here differ substantially from the true structure of the region.

Additionally, the results of Section 3. as well the comparisons of seasonal TWS between PREM and the local LITHO1.0 models point out that as the spatial-scale of surface loading becomes increasingly fine, sensitivity to Earth structure can have a significant effect on estimates of TWS. As such, we find current approaches utilized to estimate TWS within mountain and agricultural provinces of the western U.S. are subject to minor biases associated with assumed Earth structure as many of these provinces span large areas within the region. However, as it becomes of interest to use geodetic methods to constrain storage within individual watersheds and even small areas, lack of knowledge of the local crust and upper mantle structure of a region may yield estimates of TWS that are significantly biased by choice of Earth model. Moreover, as GNSS networks in the western U.S. become increasingly dense, and non-hydrologic processes that deform the Earth are more accurately modeled and removed from GNSS time series, uncertainties of GNSS-inferred TWS estimates associated with Earth structure may become increasingly significant.

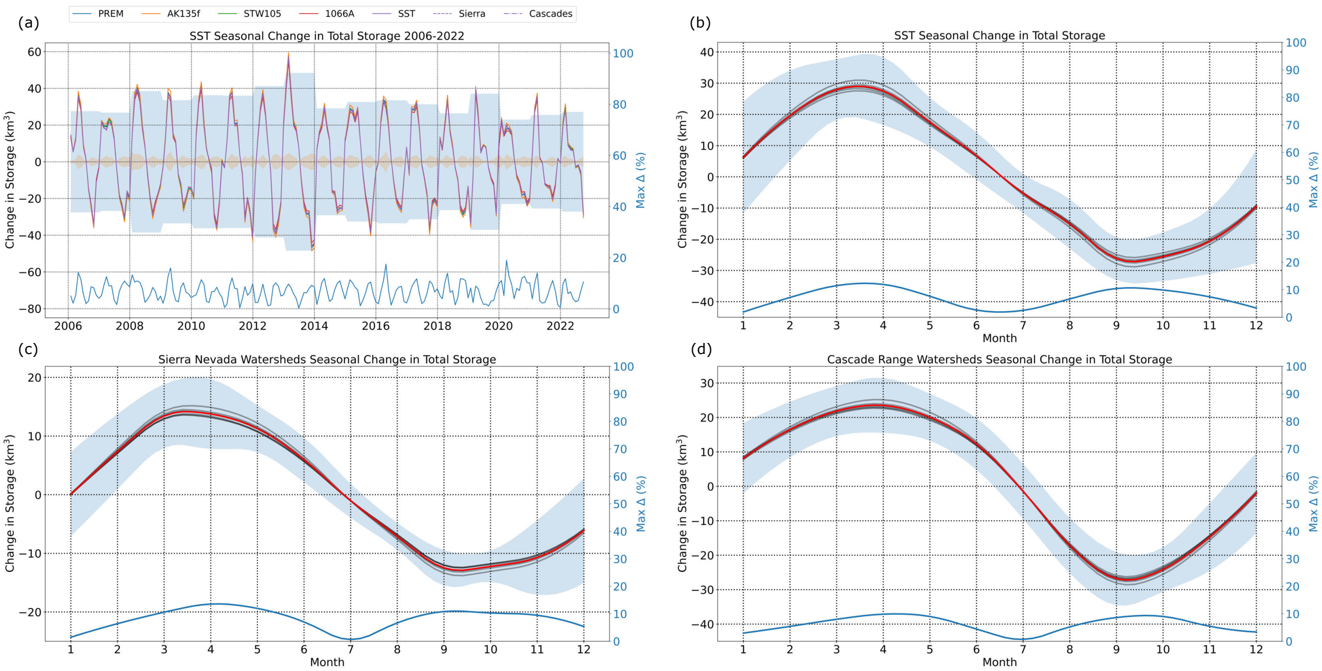

Figure 7. Estimated change in volumetric storage (km^3) between January 2006 and September 2022 in the (a) SST River Basin. The yellow shaded area depicts the maximum difference in estimated storage between the Earth models used here. The solid blue line represents the maximum percentage difference between estimates of storage relative to that year's annual amplitude (blue shaded area). (b-d) Multi-year monthly stacked estimates of storage within the SST River Basin, Sierra Nevada of California, and the Cascade Range of Washington, Oregon, and northern California. The red line depicts the estimated mean seasonal fluctuation in storage within each region considering estimates derived from the seven Earth models used here (light gray lines). The light blue line depicts the maximum percentage difference between residuals derived from the set of Earth models considered here relative to the estimated mean seasonal amplitude of all models. The blue shaded area depicts the standard deviation of seasonal storage considering the full time series of monthly TWS estimates between January 2006 and September 2022.

4 Predicted Global Hydrologic Loading

While the previous sections provide an awareness of the scale dependence of error in GNSS-inferred TWS estimates and the sensitivity of seasonal TWS estimates in the western U.S. to assumed Earth structure, we have only considered the effect of assumed Earth structure for surface loads that are invariant in time (Section 2.) or oscillate at an annual time scale (Section 3.). However, in many regions, hydrologic and cryospheric reservoirs have seen significant changes in storage over the past several decades associated with modern shifts in climate and an increasing reliance on groundwater to meet human needs as the global population grows (e.g. Wada et al., 2010; Paolo et al., 2015; Rodell et al., 2018; Seo et al., 2023). As such, loading and unloading of the solid Earth associated with long-term storage variations produces measurable changes in the Earth's figure and gravity field which can be used to constrain decreases in groundwater storage associated with multi-year drought (e.g. Argus et al., 2017; Liu et al., 2022; Argus et al., 2022), mass loss from the planet's ice sheet's and glaciers (e.g. Wouters et al., 2019; Sasgen et al., 2020), and changes in global mean sea level (e.g. Reager et al., 2016; Jeon et al., 2018).

In addition to constraining variations in storage within natural reservoirs, observations of surface displacement may be compared with predictions (typically assuming a radially varying Earth model) to characterize deformation of the Earth's surface produced by the Earth's elastic response to modern day changes in the distribution of surface and near surface mass and the viscous response to much older loading/unloading events through processes such as glacial isostatic adjustment. Through such comparisons, it is possible to acquire unique information about the viscosity structure of the Earth's mantle (Velicogna & Wahr, 2002; Nield et al., 2014; Koulali et al., 2022). Furthermore, by separating observations of surface displacement produced by past and present loading, area-specific sea level rise may be attributed to the unique Earth system process producing mass redistribution as well as motion of the Earth's surface (Zanchettin et al., 2021; Ziegler et al., 2022).

As we saw in previous sections, in areas experiencing relatively high amplitude changes in storage (i.e., the source of surface loading/unloading is large), there is an increased sensitivity to the choice of Earth model used to model displacements produced by an applied load. As such, in regions that have experienced large-scale and systematic changes in storage within surface and near-surface reservoirs over the past several decades, such as the Greenland ice sheet, we presume that predictions of elastic displacement may be particularly sensitive to choice of Earth model. To explore this further, we next consider forward model predictions of elastic displacement produced by global variations in storage within natural reservoirs over the past two decades.

4.1 Effect of Earth Structure on Predicted Vertical Land Motion

Using *LoadDef* (Martens et al., 2019), we model surface displacements produced by global hydrologic loading derived from liquid water equivalent estimates of the Jet Propulsion Laboratory's monthly GRACE mascon solution (version RL06.1M) (Landerer et al., 2020; Watkins et al., 2015; Wiese et al., 2016) over a global 1°x1° grid. We model vertical displacement of the Earth's surface over the past two decades (spanning April 2002 to September 2022) to identify regions experiencing strong multi-decadal changes in storage, and to estimate the discrepancies in predicted displacement that can be introduced by assuming different models for Earth structure. Predictions of global hydrologic loading are computed assuming commonly used Earth models: PREM, AK135f, STW105, and 1066A. All predictions reported here are considered relative to April, 2002.

Figure. 8 shows predictions of global vertical displacement for select months between April, 2002 and September 2022. Regions that have observed considerable loss of mass stored within natural reservoirs over the past two decades such as the Greenland ice sheet, western Antarctica, and southeastern Alaska exhibit relatively large uplift. For example, we find western portions of the Greenland ice sheet are predicted to have risen between 160 and 180 mm at a mean rate of 8.3 mm/yr since April, 2002 through the Earth's elastic response to pervasive loss of ice stored within the ice sheet, consistent with previous findings (e.g. Tapley et al., 2019). Conversely, regions that have observed increases in hydrologic storage relative to the start of the time series exhibit subsidence (e.g., Amazon river basin in April 2022).

Figure. 8 b-d show vector differences between pairs of forward models using different globally averaged estimates of Earth structure. The largest discrepancies between predictions are located in polar regions where significant unloading of the Earth's surface has occurred over the past two decades due to the loss of ice mass and can be as large as 20 mm for select forward model pairs. Relatively large discrepancies between forward model predictions also exist in regions that have seen increases in storage within hydrologic reservoirs over the past two decades, such as eastern Antarctica and the western Zambezi basin of Africa (Rodell et al., 2018). However, the increases in storage within these regions, and thus predicted displacement and differences between predictions derived from various Earth models, are smaller in amplitude compared to mass deficits in regions containing large ice sheets and glaciers. Vector differences for other pairs of Earth models are provided in the supplemental information (Fig. S20).

To further investigate the effect of Earth structure on predictions of vertical displacement associated with long-term changes in storage, we focus on regions that exhibit the largest discrepancies between forward model predictions at the end of the study period (Fig. 8). Namely, we consider the Greenland ice sheet, western Antarctica, and southeastern Alaska, as these regions have all experienced considerable losses of mass stored within ice sheets or glaciers as a result of modern changes in global climate producing significant uplift of the Earth's surface. Time series of predicted vertical displacement for individual synthetic GPS stations (denoted by inverted triangles in Fig. 9a) located within our regions of interest are displayed in Figure. 9b-d.

Predictions of vertical displacement for the Greenland ice sheet and western Antarctica demonstrate substantial linear trends over the past two decades, attributed to continuous ice loss within these regions, with minor variability in certain years (Fig. 9b, 9c). Since April 2002, these regions are predicted to have experienced between 161 to 181 and 186 to 205 mm of uplift respectively. In both regions, the largest discrepancies in predictions are between AK135f and 1066A, which differ by over 19 and 18 mm respectively by September 2022 and deviate from each other at a rate of nearly 1 mm per year (Fig. S20a, S20b). Conversely, the smallest discrepancies in predicted displacement are found between PREM and STW105, which differ by less than 4 mm within both regions by September 2022. Similarly, predictions in southeastern Alaska are characterized by a significant linear trend associated with mass loss from glaciers within the region, although there is also a notable seasonal oscillation in predicted displacement attributed to annual precipitation patterns (Fig. 9d). Since April 2002, southeastern Alaska is predicted to have been uplifted between 79 and 85 mm over the past two decades. As with the other regions considered here, the largest discrepancies are between AK135f and 1066A, with a maximum difference of approximately 5 mm (Fig. S20c), while the smallest discrepancies are between PREM and AK135f, with a difference of 1 mm.

We note two important findings depicted in Fig. 9 and their associated implications. First, as changes in storage within hydrologic and cryospheric reservoirs are sustained over significant periods of time, acting as an increasingly large source of surface loading/unloading, discrepancies in predicted vertical displacement between pairs of forward models become increasingly significant. For example, differences in predicted uplift of the Greenland ice sheet between forward models using PREM and AK135f increase from approximately 2.5 mm in April, 2009 to over 8 mm in April, 2022 (Fig. S20). As such, when utilizing observations of surface loading to constrain changes in storage within

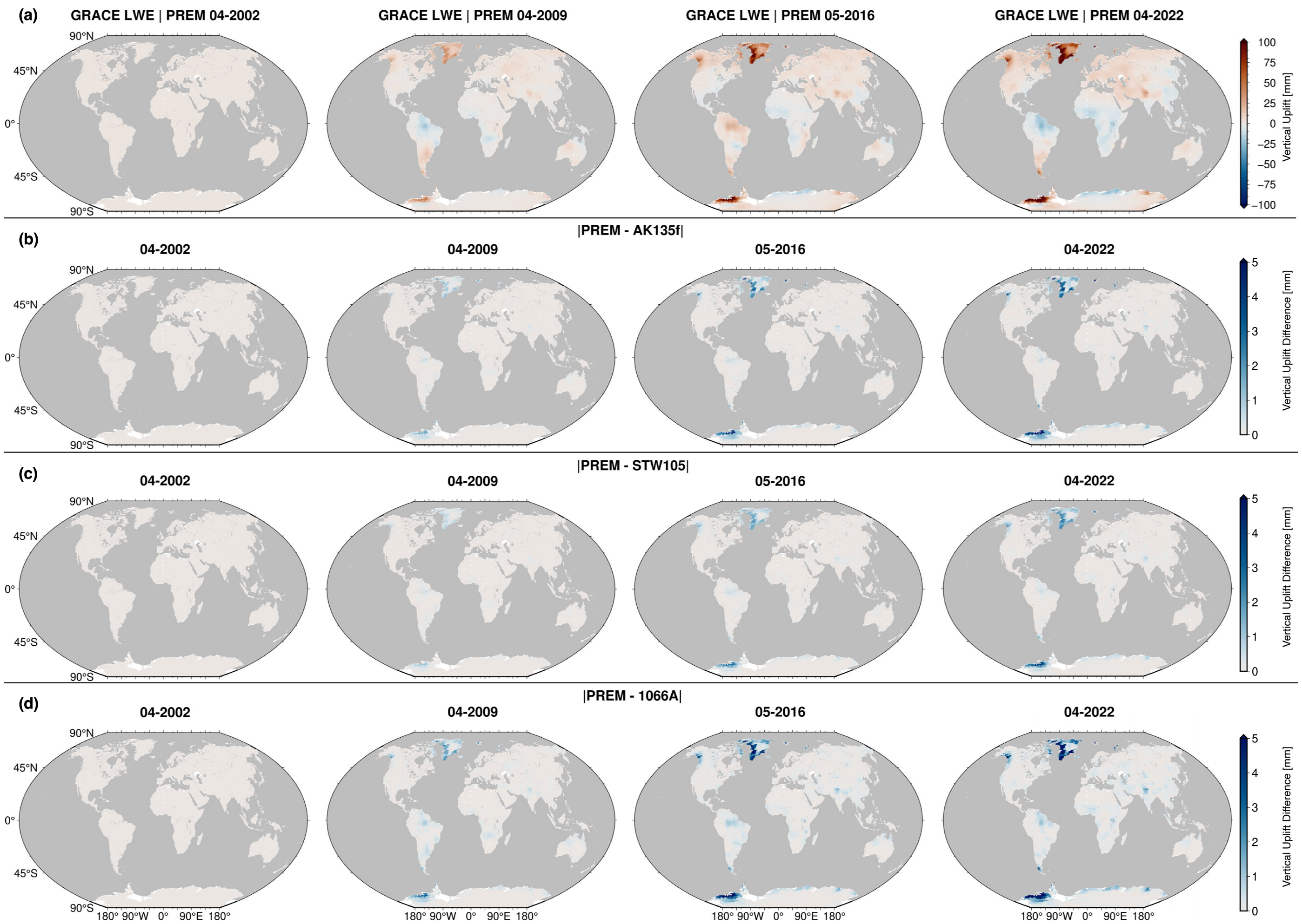

Figure 8. (a) Predicted vertical displacement for select months between April 2002 and April 2022 derived through the convolution of the LGFs of PREM with liquid water equivalent estimates of the Jet Propulsion Laboratory's monthly GRACE mascon solution (version RL06.1M) for a global 1°x1°. Predicted displacements are considered relative to April 2002. Note: The upper right color bar saturates beyond a value of 100 mm. Vector differences between pairs of predicted hydrologic-induced displacements for select Earth models: (b) PREM and AK135f, (c) PREM and STW105, and (d) PREM and 1066A. The lower right color bars depict the hydrologic-induced displacement amplitude difference between pairs of Earth models. Note: The lower right color bars saturate beyond a value of 5 mm.

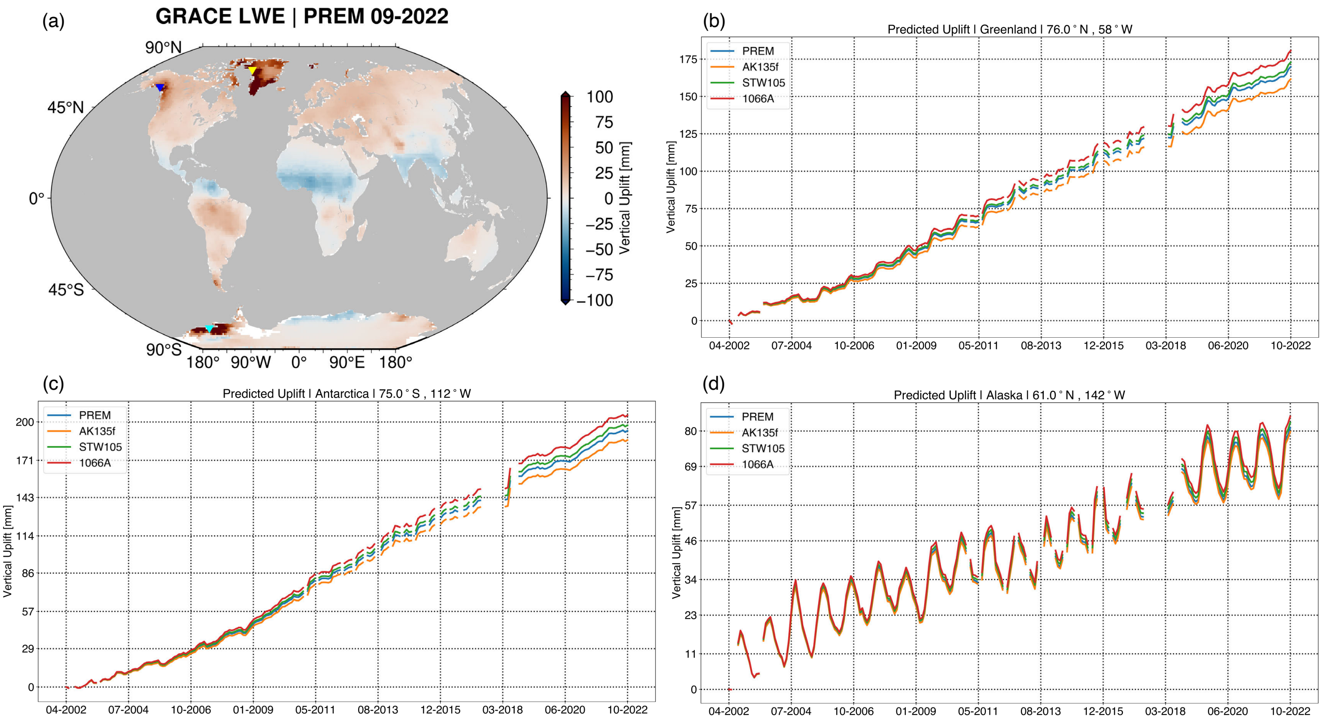

Figure 9. (a) Predicted vertical displacement for the month of September 2022. Inverted triangles represent sampling locations for the displacement time series depicted in panels (b-d). Note: The color bar saturates beyond a value of 100 mm. Predictions between April 2002 and September 2022 for select Earth models at : (b) 76.0° N, 58° W on the western portion of the Greenland Ice Sheet, (c) 75° S, 112° W in western Antarctica, and (d) 61.0° N, 142° W in south-eastern Alaska. Gaps in predicted VLM depicted here represent data gaps in the time series of GRACE and GRACE-FO.

natural reservoirs occurring over years to decades (e.g., deglaciation, drought, groundwater depletion), the choice of Earth model becomes increasingly import as the source of surface loading becomes progressively large. As a result, storage estimates and associated interpretations may differ significantly owing to choice of Earth model. Similarly, as many regions exhibit long-term vertical deformation produced by secular trends in hydrology and glacial isostatic adjustment, prediction and subsequent removal of elastic deformation produced by hydrologic loading may yield widely variable estimates of the Earth's viscous deformation response to past loading.

Second, we find that differences in predictions of long-term vertical displacement can be significantly larger than the current observational uncertainty of GNSS ($\sim$ 1 mm), especially in regions containing large ice sheets and glaciers. While such discrepancies pose challenges in using observations of surface displacement to constrain variations in storage within such regions, immense progress has been made over the past several decades to provide accurate estimates of mass change within the Earth's ice sheets and glaciers using satellite altimetry (e.g. Spada et al., 2012; Smith et al., 2020) and gravity field observations (e.g. Chen et al., 2006; Sasgen et al., 2019). As such, we propose that comparison of predicted and observed surface displacement within these regions, may provide a unique opportunity to differentiate between suitable models for regional crust and mantle structure. Such information would not only provide an independent approach to constrain the interior structure of the Earth, complimenting estimates derived from seismic observations, but would also allow for better characterization of deformation produced by glacial isostatic adjustment within these regions if deformation produced by modern unloading can be accurately modeled and removed.

5 Conclusion

Here, we explore the sensitivity of terrestrial water storage estimates derived from observations of surface mass loading to assumed Earth structure. Through a series of synthetic loading tests, we find that as the spatial scale of surface loading becomes progressively smaller, estimates of terrestrial water storage can have errors associated with the choice of Earth model nearly as large as 80%. As such, it may not be possible to make accurate estimates of variations in storage using geodetic methods at relatively fine spatial scales (<10 km) without comprehensive knowledge of a region's local crustal structure, limiting the use of geodetic observations to constrain variations in storage within relatively small hydrologic reservoirs, such as a lake or artificial reservoir. However, our results indicate that surface loads on the order of tens to hundreds of kilometers in size are well recovered, even if the Earth model used to estimate TWS differs from the Earth's interior structure.

To determine the effect of Earth structure in a region particularly relevant in the field of hydrogeodesy, we estimated seasonal variations in GNSS-inferred terrestiral water storage within the western U.S. between January 2006 and September 2022 using multiple global and regional models for the structure of the Earth. In general, we find the largest discrepancies in estimates of seasonal TWS within mountainous regions of the western U.S., where the seasonal accumulation of rain and snow act as a large source of surface loading, enhancing sensitivities to structure relative to areas with small seasonal fluctuations in storage. Similarly, we find sensitivities to Earth structure are maximized in spring and fall months when many natural reservoirs are at their annual maximum/minimum. Overall, we find that assumed Earth structure has a small bias on estimates of seasonal TWS within mountain and agricultural provinces of the western U.S., yielding estimates that can differ by over 13%.

In addition, to consider the effect of assumed Earth structure on estimating storage and/or surface displacement associated with variations in storage within hydrologic and cryospheric reservoirs occurring over several decades, we compared predictions of global hydrologic loading over the past two decades assuming globally averaged estimates of Earth structure. Our results indicate that estimates of surface loading are particularly sensitive to choice of Earth model in regions experiencing large-scale and systematic variations in storage within natural reservoirs, such as the Earth's ice sheets and glaciers where predictions of uplift associated with ice loss can differ by as much as 20 mm, substantially larger than the current observational uncertainty of GNSS. As a result, we postulate that observations of the Earth's elastic response to mass loss from ice sheets and glaciers may provide valuable information which may be used to constrain the elastic and density structure of the crust and upper mantle.

Open Research Section

Solution files for the synthetic tests, stations used for the inversion in Section 3, and estimates of seasonal water storage within the western U.S. for each month from January 2006 and September 2022 are publicly available at https://figshare.com/s/d191705ec826efdda812. Jet Propulsion Laboratory's GRACE Mascon solution can be accessed at https://grace.jpl.nasa.gov/data/get-data/ jpl_global_mascons/. GPS positions processed at the Nevada Geodetic Laboratory are available at http://geodesy.unr.edu/gps_timeseries/tenv3/IGS14/. The *LoadDef* software suite can be accessed at https://github.com/hrmartens/LoadDef.

Acknowledgments

This material is based upon work supported by NASA Earth Surface and Interior grant 80NSSC19K0361 and National Science Foundation grants EAR-2218194 and EAR-2021637. A portion of this material is based on services provided by the GAGE Facility, operated by the EarthScope Consortium, with support from the National Science Foundation, the National Aeronautics and Space Administration, and the U.S. Geological Survey under NSF Cooperative Agreement EAR-1724794. We express gratitude to the processing group at the Nevada Geodetic Laboratory for providing publicly available processed GPS data. MJS wishes to thank colleagues at Scripps Institution of Oceanography at UC San Diego for their hospitality and fruitful discussions during the summer of 2023. Figures presented in this manuscript were produced using Generic Mapping Tools (Wessel et al., 2019) and Matplotlib (Hunter, 2007).

References

Alterman, Z., Jarosch, H., & Pekeris, C. L. (1961, 12). Propagation of rayleigh waves in the earth. *Geophysical Journal International*, *4*, 219-241. doi: 10.1111/j.1365-246X.1961.tb06815.x

Argus, D. F., Fu, Y., & Landerer, F. W. (2014, 3). Seasonal variation in total water storage in california inferred from gps observations of vertical land motion. *Geophysical Research Letters*, *41*, 1971-1980. doi: 10.1002/2014GL059570

Argus, D. F., Landerer, F. W., Wiese, D. N., Martens, H. R., Fu, Y., Famiglietti, J. S., ... Watkins, M. M. (2017, 12). Sustained water loss in california's mountain ranges during severe drought from 2012 to 2015 inferred from gps. *Journal of Geophysical Research: Solid Earth*, *122*. doi: 10.1002/2017JB014424

Argus, D. F., Martens, H. R., Borsa, A. A., Knappe, E., Wiese, D. N., Alam, S., ... Gardiner, W. P. (2022, 11). Subsurface water flux in california's central valley and its source watershed from space geodesy. *Geophysical Research Letters*, *49*. doi: 10.1029/2022GL099583

Aster, R. C., Borchers, B., & Thurber, C. H. (2019). *Parameter estimation and inverse problems*. Elsevier. doi: 10.1016/C2015-0-02458-3

Blewitt, G. (2003, 2). Self-consistency in reference frames, geocenter definition, and surface loading of the solid earth. *Journal of Geophysical Research: Solid Earth*, *108*. doi: 10.1029/2002JB002082

Blewitt, G., Hammond, W., & Kreemer, C. (2018, 9). Harnessing the gps data explosion for interdisciplinary science. *Eos*, *99*. doi: 10.1029/2018EO104623

Borsa, A. A., Agnew, D. C., & Cayan, D. R. (2014, 9). Ongoing drought-induced uplift in the western united states. *Science*, *345*, 1587-1590. doi: 10.1126/science.1260279

Brown, T. C., Hobbins, M. T., & Ramirez, J. A. (2008, 12). Spatial distribution of water supply in the coterminous united states ¡sup¿1¡/sup¿. *JAWRA Journal of the American Water Resources Association*, *44*, 1474-1487. doi: 10.1111/j.1752-1688.2008.00252.x

Carlson, G., Werth, S., & Shirzaei, M. (2022, 3). Joint inversion of gnss and grace for terrestrial water storage change in california. *Journal of Geophysical Research: Solid Earth*, *127*. doi: 10.1029/2021JB023135

Chen, J. L., Wilson, C. R., & Tapley, B. D. (2006, 9). Satellite gravity measurements confirm accelerated melting of greenland ice sheet. *Science*, *313*, 1958-1960. doi: 10.1126/science.1129007

Chu, R., Schmandt, B., & Helmberger, D. V. (2012, 2). Upper mantle ¡i¿p¡/i¿ velocity structure beneath the midwestern united states derived from triplicated waveforms. *Geochemistry, Geophysics, Geosystems*, *13*, n/a-n/a. doi: 10.1029/2011GC003818

Dill, R., & Dobslaw, H. (2013, 9). Numerical simulations of global-scale high-resolution hydrological crustal deformations. *Journal of Geophysical Research: Solid Earth*, *118*, 5008-5017. doi: 10.1002/jgrb.50353

Dill, R., Klemann, V., Martinec, Z., & Tesauro, M. (2015, 8). Applying local green's functions to study the influence of the crustal structure on hydrological loading displacements. *Journal of Geodynamics*, *88*, 14-22. doi: 10.1016/j.jog.2015.04.005

Dziewonski, A. M., & Anderson, D. L. (1981, 6). Preliminary reference earth model. *Physics of the Earth and Planetary Interiors*, *25*, 297-356. doi: 10.1016/0031-9201(81)90046-7

Enzminger, T. L., Small, E. E., & Borsa, A. A. (2018, 1). Accuracy of snow water equivalent estimated from gps vertical displacements: A synthetic loading case study for western u.s. mountains. *Water Resources Research*, *54*, 581-599. doi: 10.1002/2017WR021521

Enzminger, T. L., Small, E. E., & Borsa, A. A. (2019, 11). Subsurface water dominates sierra nevada seasonal hydrologic storage. *Geophysical Research Letters*, *46*, 11993-12001. doi: 10.1029/2019GL084589

Farrell, W. E. (1972, 8). Deformation of the earth by surface loads. *Reviews of Geophysics*, *10*, 761-797. doi: 10.1029/RG010i003p00761

Fu, Y., Argus, D. F., & Landerer, F. W. (2015, 1). Gps as an independent measurement to estimate terrestrial water storage variations in washington and oregon. *Journal of Geophysical Research: Solid Earth*, *120*, 552-566. doi: 10.1002/2014JB011415

Gilbert, F., & Dziewonski, A. M. (1975, 3). An application of normal mode theory to the retrieval of structural parameters and source mechanisms from seismic spectra. *Philosophical Transactions of the Royal Society of London. Series A, Mathematical and Physical Sciences*, *278*, 187-269. doi: 10.1098/rsta.1975.0025

Grand, S. P., & Helmberger, D. V. (1984, 12). Upper mantle shear structure beneath the northwest atlantic ocean. *Journal of Geophysical Research: Solid Earth*, *89*, 11465-11475. doi: 10.1029/JB089iB13p11465

Guo, J. Y., Li, Y. B., Huang, Y., Deng, H. T., Xu, S. Q., & Ning, J. S. (2004, 10). Green's function of the deformation of the earth as a result of atmospheric loading. *Geophysical Journal International*, *159*, 53-68. doi: 10.1111/j.1365-246X.2004.02410.x

Hansen, P. C. (1992, 12). Analysis of discrete ill-posed problems by means of the l-curve. *SIAM Review*, *34*, 561-580. doi: 10.1137/1034115

Herring, T. A., Melbourne, T. I., Murray, M. H., Floyd, M. A., Szeliga, W. M., King, R. W., ... Wang, L. (2016, 12). Plate boundary observatory and related networks: Gps data analysis methods and geodetic products. *Reviews of Geophysics*, *54*, 759-808. doi: 10.1002/2016RG000529

Hunter, J. D. (2007). Matplotlib: A 2d graphics environment. *Computing in Science & Engineering*, *9*, 90-95. doi: 10.1109/MCSE.2007.55

Ito, T., & Simons, M. (2011, 5). Probing asthenospheric density, temperature, and elastic moduli below the western united states. *Science*, *332*, 947-951. doi: 10.1126/science.1202584

Jeon, T., Seo, K.-W., Youm, K., Chen, J., & Wilson, C. R. (2018, 9). Global sea level change signatures observed by grace satellite gravimetry. *Scientific Reports*, *8*, 13519. doi: 10.1038/s41598-018-31972-8

Kennett, B. L. N., Engdahl, E. R., & Buland, R. (1995, 7). Constraints on seismic velocities in the earth from traveltimes. *Geophysical Journal International*, *122*, 108-124. doi: 10.1111/j.1365-246X.1995.tb03540.x

Koulali, A., Whitehouse, P. L., Clarke, P. J., van den Broeke, M. R., Nield, G. A., King, M. A., ... Wilson, T. (2022, 2). Gps-observed elastic deformation due to surface mass balance variability in the southern antarctic peninsula. *Geophysical Research Letters*, *49*. doi: 10.1029/2021GL097109

Kreemer, C., Blewitt, G., & Maerten, F. (2006). Co- and postseismic deformation of the 28 march 2005 nias ¡i¿m¡/i¿ ¡sub¿ ¡i¿w¡/i¿ ¡/sub¿ 8.7 earthquake from continuous gps data. *Geophysical Research Letters*, *33*, L07307. doi: 10.1029/2005GL025566

Kreemer, C., Hammond, W. C., & Blewitt, G. (2018, 5). A robust estimation of the 3-d intraplate deformation of the north american plate from gps. *Journal of Geophysical Research: Solid Earth*, *123*, 4388-4412. doi: 10.1029/2017JB015257

Kustowski, B., Ekström, G., & Dziewoński, A. M. (2008, 6). Anisotropic shear-wave velocity structure of the earth's mantle: A global model. *Journal of Geophysical Research*, *113*, B06306. doi: 10.1029/2007JB005169

Landerer, F. W., Flechtner, F. M., Save, H., Webb, F. H., Bandikova, T., Bertiger, W. I., ... Yuan, D. (2020, 6). Extending the global mass change data record: Grace follow-on instrument and science data performance. *Geophysical Research Letters*, *47*. doi: 10.1029/2020GL088306

Lettenmaier, D. P., & Famiglietti, J. S. (2006, 11). Water from on high. *Nature*, *444*, 562-563. doi: 10.1038/444562a

Liu, P.-W., Famiglietti, J. S., Purdy, A. J., Adams, K. H., McEvoy, A. L., Reager, J. T., ... Rodell, M. (2022, 12). Groundwater depletion in california's central valley accelerates during megadrought. *Nature Communications*, *13*, 7825. doi: 10.1038/s41467-022-35582-x

Martens, H. R., Rivera, L., & Simons, M. (2019, 2). Loaddef: A python-based toolkit to model elastic deformation caused by surface mass loading on spherically symmetric bodies. *Earth and Space Science*, *6*, 311-323. doi: 10.1029/2018EA000462

Martens, H. R., Rivera, L., Simons, M., & Ito, T. (2016, 5). The sensitivity of surface mass loading displacement response to perturbations in the elastic structure of the crust and mantle. *Journal of Geophysical Research: Solid Earth*, *121*, 3911-3938. doi: 10.1002/2015JB012456

Martens, H. R., & Simons, M. (2020, 10). A comparison of predicted and observed ocean tidal loading in alaska. *Geophysical Journal International*, *223*, 454-470. doi: 10.1093/gji/ggaa323

Martens, H. R., Simons, M., Owen, S., & Rivera, L. (2016, 6). Observations of ocean tidal load response in south america from subdaily gps positions. *Geophysical Journal International*, *205*, 1637-1664. doi: 10.1093/gji/ggw087

Milliner, C., Materna, K., Bürgmann, R., Fu, Y., Moore, A. W., Bekaert, D., ... Argus, D. F. (2018, 9). Tracking the weight of hurricane harvey's stormwater using gps data. *Science Advances*, *4*. doi: 10.1126/sciadv.aau2477

Montagner, J.-P., & Kennett, B. L. N. (1996, 4). How to reconcile body-wave and normal-mode reference earth models. *Geophysical Journal International*, *125*, 229-248. doi: 10.1111/j.1365-246X.1996.tb06548.x

Nield, G. A., Barletta, V. R., Bordoni, A., King, M. A., Whitehouse, P. L., Clarke, P. J., ... Berthier, E. (2014, 7). Rapid bedrock uplift in the antarctic peninsula explained by viscoelastic response to recent ice unloading. *Earth and Planetary Science Letters*, *397*, 32-41. doi: 10.1016/j.epsl.2014.04.019

Paolo, F. S., Fricker, H. A., & Padman, L. (2015, 4). Volume loss from antarctic ice shelves is accelerating. *Science*, *348*, 327-331. doi: 10.1126/science.aaa0940

Pasyanos, M. E., Masters, T. G., Laske, G., & Ma, Z. (2014, 3). Litho1.0: An updated crust and lithospheric model of the earth. *Journal of Geophysical Research: Solid Earth*, *119*, 2153-2173. doi: 10.1002/2013JB010626

Peltier, W. R., Argus, D. F., & Drummond, R. (2018, 2). Comment on "an assessment of the ice-6g_c (vm5a) glacial isostatic adjustment model" by purcell et al. *Journal of Geophysical Research: Solid Earth*, *123*, 2019-2028. doi: 10.1002/2016JB013844

Reager, J. T., Gardner, A. S., Famiglietti, J. S., Wiese, D. N., Eicker, A., & Lo, M.-H. (2016, 2). A decade of sea level rise slowed by climate-driven hydrology. *Science*, *351*, 699-703. doi: 10.1126/science.aad8386

Rodell, M., Famiglietti, J. S., Wiese, D. N., Reager, J. T., Beaudoing, H. K., Landerer, F. W., & Lo, M.-H. (2018, 5). Emerging trends in global freshwater availability. *Nature*, *557*, 651-659. doi: 10.1038/s41586-018-0123-1

Sasgen, I., Konrad, H., Helm, V., & Grosfeld, K. (2019, 1). High-resolution mass trends of the antarctic ice sheet through a spectral combination of satellite gravimetry and radar altimetry observations. *Remote Sensing*, *11*, 144. doi: 10.3390/rs11020144

Sasgen, I., Wouters, B., Gardner, A. S., King, M. D., Tedesco, M., Landerer, F. W., ... Fettweis, X. (2020, 8). Return to rapid ice loss in greenland and record loss in 2019 detected by the grace-fo satellites. *Communications Earth & Environment*, *1*, 8. doi: 10.1038/s43247-020-0010-1

Seo, K., Ryu, D., Eom, J., Jeon, T., Kim, J., Youm, K., ... Wilson, C. R. (2023, 6). Drift of earth's pole confirms groundwater depletion as a significant contributor to global sea level rise 1993–2010. *Geophysical Research Letters*, *50*. doi: 10.1029/2023GL103509

Skøien, J. O., Blöschl, G., & Western, A. W. (2003, 10). Characteristic space scales and timescales in hydrology. *Water Resources Research*, *39*. doi: 10.1029/2002WR001736

Smith, B., Fricker, H. A., Gardner, A. S., Medley, B., Nilsson, J., Paolo, F. S., ... Zwally, H. J. (2020, 6). Pervasive ice sheet mass loss reflects competing ocean and atmosphere processes. *Science*, *368*, 1239-1242. doi: 10.1126/science.aaz5845

Spada, G., Ruggieri, G., Sørensen, L. S., Nielsen, K., Melini, D., & Colleoni, F. (2012, 6). Greenland uplift and regional sea level changes from icesat observations and gia modelling. *Geophysical Journal International*, *189*, 1457-1474. doi: 10.1111/j.1365-246X.2012.05443.x

Tapley, B. D., Watkins, M. M., Flechtner, F., Reigber, C., Bettadpur, S., Rodell, M., ... Velicogna, I. (2019, 5). Contributions of grace to understanding climate change. *Nature Climate Change*, *9*, 358-369. doi: 10.1038/s41558-019-0456-2

Velicogna, I., & Wahr, J. (2002, 12). Postglacial rebound and earth's viscosity structure from grace. *Journal of Geophysical Research: Solid Earth*, *107*, ETG 17-1-ETG 17-12. doi: 10.1029/2001JB001735

Wada, Y., van Beek, L. P. H., van Kempen, C. M., Reckman, J. W. T. M., Vasak, S., & Bierkens, M. F. P. (2010, 10). Global depletion of groundwater resources. *Geophysical Research Letters*, *37*, n/a-n/a. doi: 10.1029/2010GL044571

Wahr, J., Swenson, S., Zlotnicki, V., & Velicogna, I. (2004, 6). Time-variable gravity from grace: First results. *Geophysical Research Letters*, *31*, n/a-n/a. doi: 10.1029/2004GL019779

Wang, H., Xiang, L., Wu, P., Jia, L., Jiang, L., Shen, Q., & Steffen, H. (2015, 5). Influences of crustal thickening in the tibetan plateau on loading modeling and inversion associated with water storage variation. *Geodesy and Geodynamics*, *6*, 161-172. doi: 10.1016/j.geog.2015.05.002

Watkins, M. M., Wiese, D. N., Yuan, D., Boening, C., & Landerer, F. W. (2015, 4). Improved methods for observing earth's time variable mass distribution with grace using spherical cap mascons. *Journal of Geophysical Research: Solid Earth*, *120*, 2648-2671. doi: 10.1002/2014JB011547

Wessel, P., Luis, J. F., Uieda, L., Scharroo, R., Wobbe, F., Smith, W. H. F., & Tian, D. (2019, 11). The generic mapping tools version 6. *Geochemistry, Geophysics, Geosystems*, *20*, 5556-5564. doi: 10.1029/2019GC008515

Wiese, D. N., Landerer, F. W., & Watkins, M. M. (2016, 9). Quantifying and reducing leakage errors in the jpl rl05m grace mascon solution. *Water Resources Research*, *52*, 7490-7502. doi: 10.1002/2016WR019344

Wouters, B., Gardner, A. S., & Moholdt, G. (2019, 5). Global glacier mass loss during the grace satellite mission (2002-2016). *Frontiers in Earth Science*, *7*. doi: 10.3389/feart.2019.00096

Zanchettin, D., Bruni, S., Raicich, F., Lionello, P., Adloff, F., Androsov, A., ... Zerbini, S. (2021, 9). Sea-level rise in venice: historic and future trends (review article). *Natural Hazards and Earth System Sciences*, *21*, 2643-2678. doi: 10.5194/nhess-21-2643-2021

Ziegler, Y., Vishwakarma, B. D., Brady, A., Chuter, S., Royston, S., Westaway, R. M., & Bamber, J. L. (2022, 10). Can gps and grace data be used to separate past and present-day surface loading in a data-driven approach? *Geophysical Journal International*, *232*, 884-901. doi: 10.1093/gji/ggac365

Supporting Information for "Sensitivity of GNSS-Derived Estimates of Terrestrial Water Storage to Assumed Earth Structure"

Matthew J. Swarr[1], Hilary R. Martens[1], and Yuning Fu[2]

[1]Department of Geosciences, University of Montana, Missoula, MT, USA

[2]School of Earth, Environment, and Society, Bowling Green State University, Bowling Green, OH, USA

Contents of this file

Additional Supporting Information (Files uploaded separately)

Region	Sampling Location	Local Lithosphere Thickness [km]
San Joaquin River Basin	39.792° N, −121.604° W	54.553
Sacramento River Basin	37.686° N, −120.475° W	54.679
Tulare River Basin	36.155° N, −119.409° W	76.14
Northern Sierra Nevada	39.612° N, −120.879° W	50.892
Central Sierra Nevada	38.102° N, −119.864° W	51.789
Southern Sierra Nevada	36.476° N, −118.496° W	68.309
Northern Cascades	48.404° N, −121.234° W	53.937
Central Cascades	45.399° N, −121.759° W	54.491
Southern Cascades	41.014° N, −122.118° W	61.983

Table S1. Sampling locations and local lithosphere thickness of radial profiles derived from LITHO1.0 used compute the average local crust and upper mantle structure of the SST River Basin, Sierra Nevada, and Cascade Range respectively.

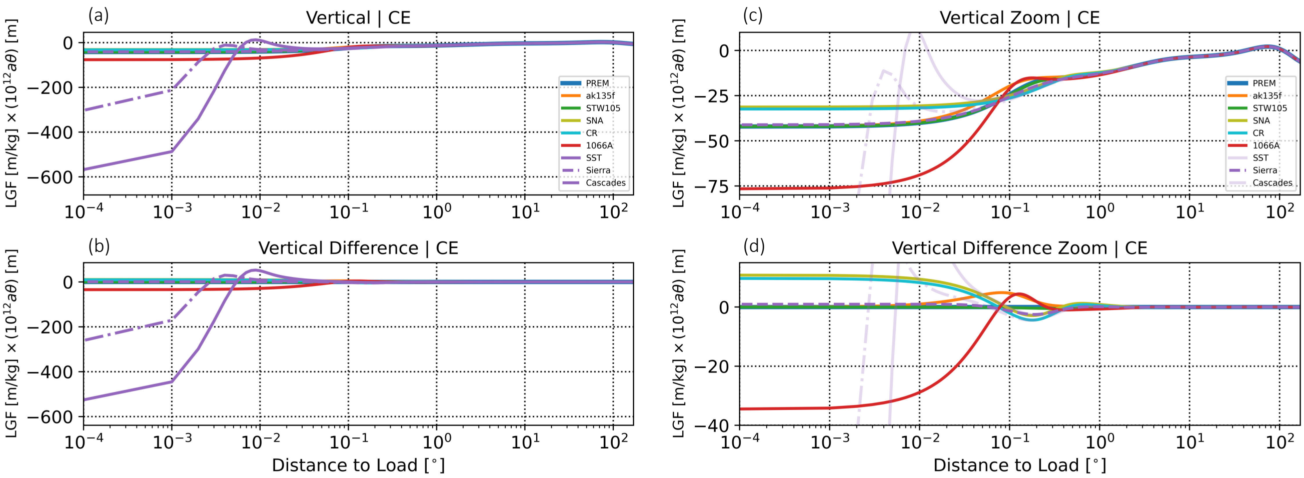

Figure S1. Displacement load Green's functions computed in the CE reference frame for PREM (blue), AK135f (orange), STW105 (green), SNA (olive), CR (cyan), 1066A (red), and average crust and upper mantle models for the San Joaquin, Sacramento, Tulare River Basin (purple), Sierra Nevada (dashed purple), and the Cascade Range (dash-dot purple). Panel (a) displays the vertical-component of the LGFs over angular distances that range from 0.001° to 170° respectively. The LGFs have been multiplied by a scaling factor $10^{12}a\theta$, where a is Earth's mean radius (units of meters) and θ represents the angular distance between the applied load and the point of observation (units of radians). Panel (b) displays the LGFs of the models considered here relative to the LGFs of PREM. Panels (c) and (d) depict a zoomed in version of the information depicted in (a) and (b).

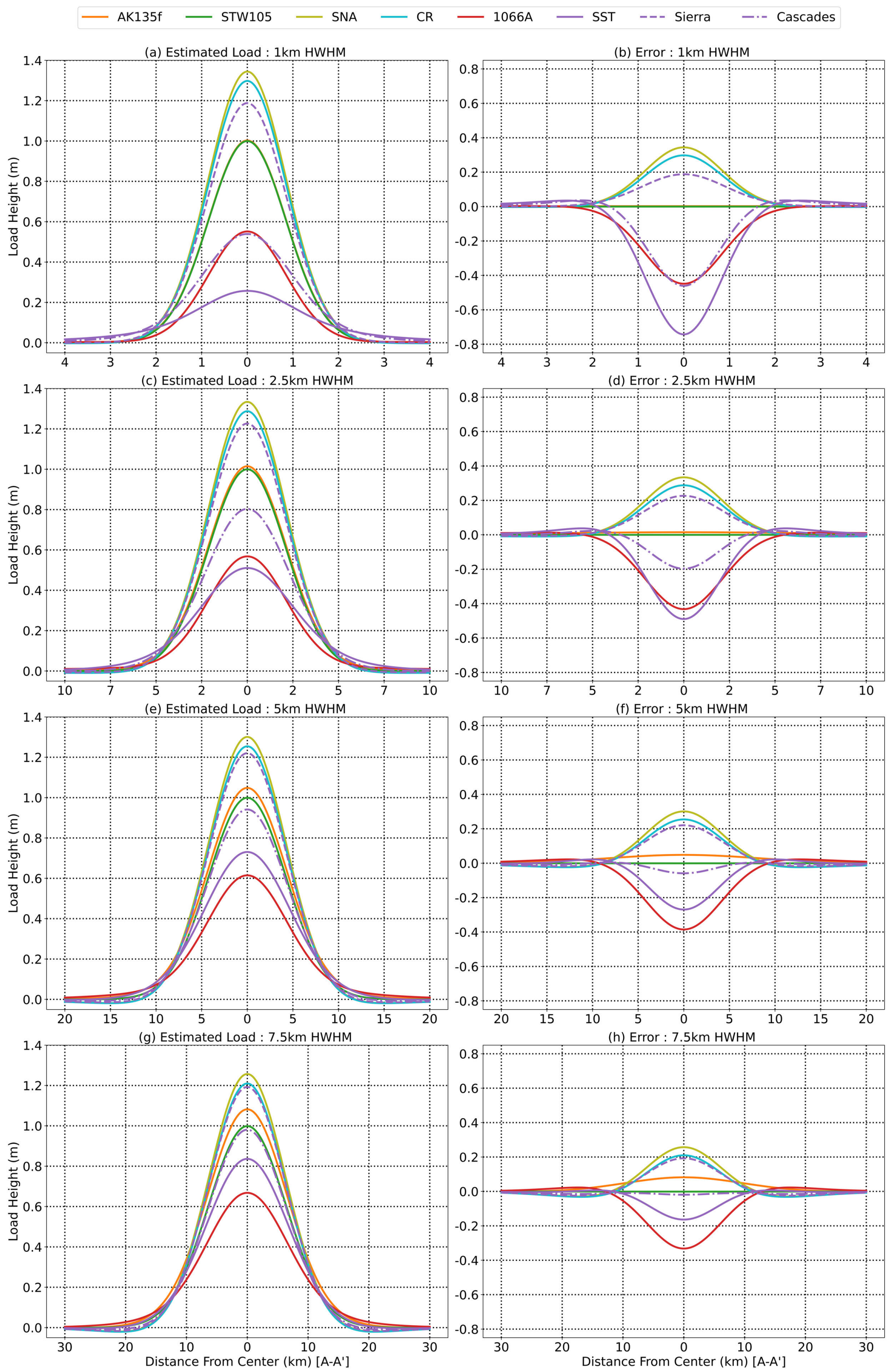

Figure S2. Estimated surface load and associated error for inversion estimates assuming the SNREI Earth structures shown in Fig. 1 along the profile A-A' in Fig. 2 for surface loads corresponding to HWHMs of: (a-b) 1 km, (c-d) 2.5 km, (e-f) 5 km, and (g-h) 7.5 km.

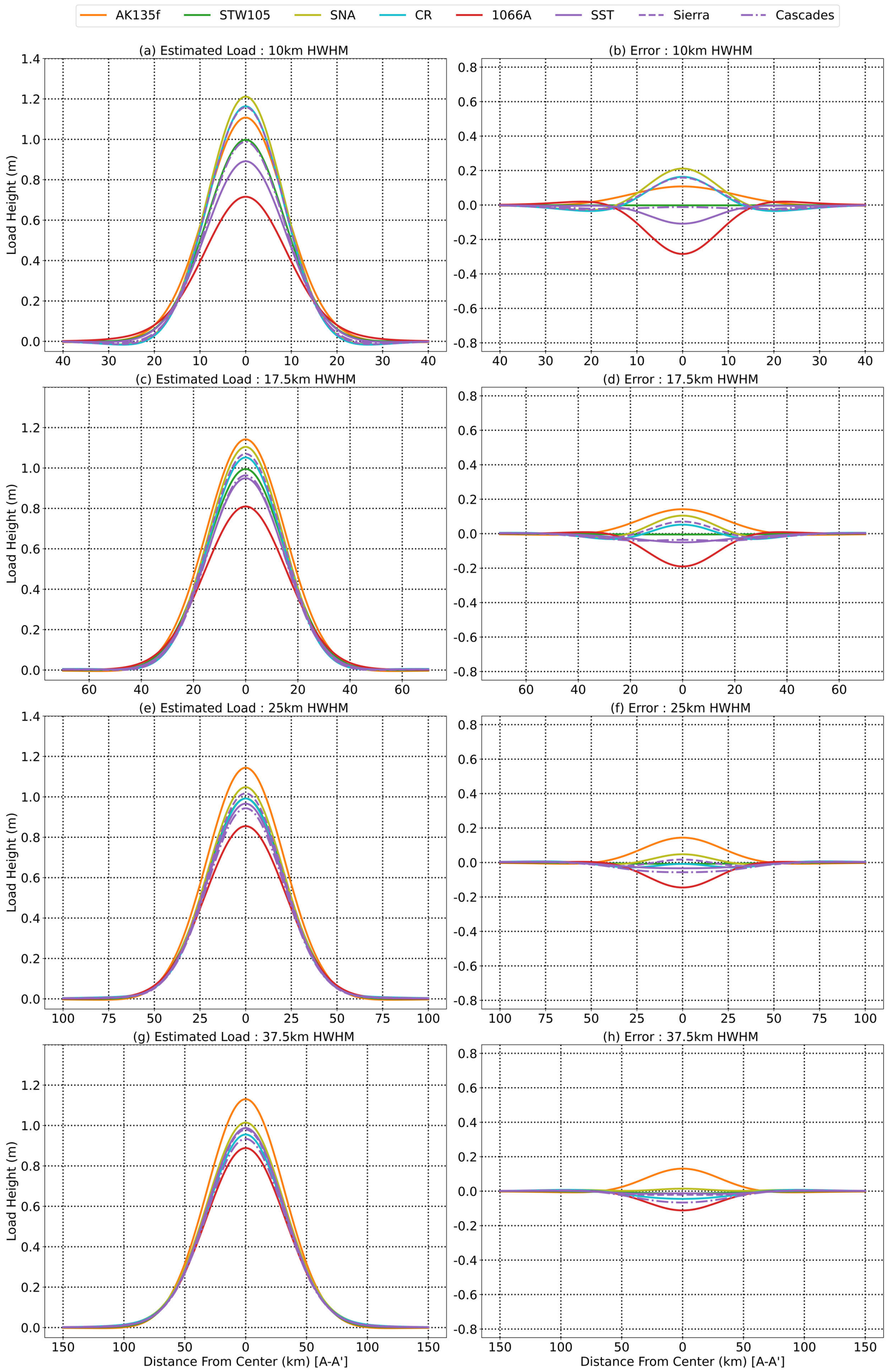

Figure S3. Estimated surface load and associated error for inversion estimates assuming the SNREI Earth structures shown in Fig. 1 along the profile A-A' in Fig. 2 for surface loads corresponding to HWHMs of: (a-b) 10 km, (c-d) 17.5 km, (e-f) 25 km, and (g-h) 37.5 km.

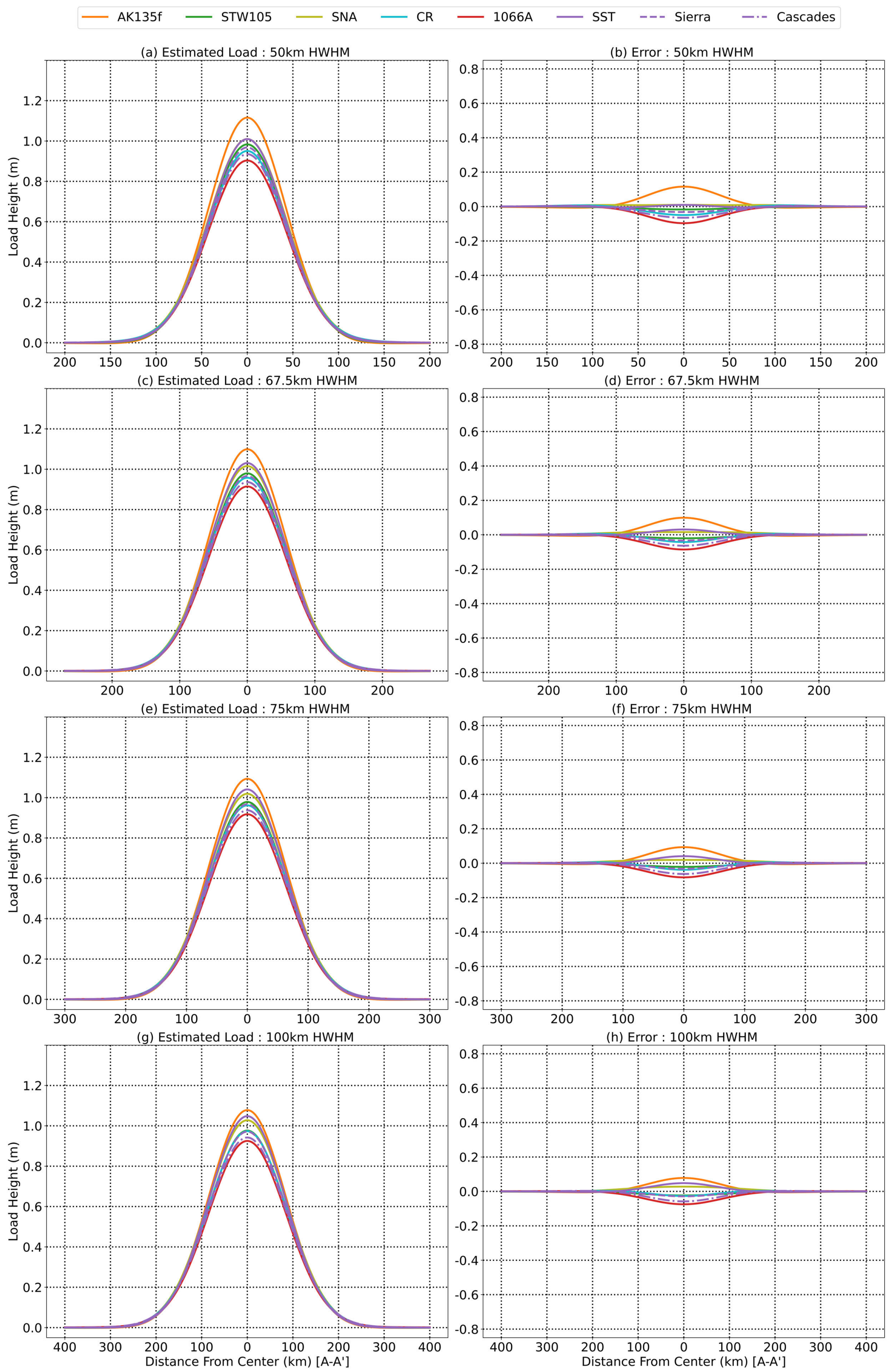

Figure S4. Estimated surface load and associated error for inversion estimates assuming the SNREI Earth structures shown in Fig. 1 along the profile A-A' in Fig. 2 for surface loads corresponding to HWHMs of: (a-b) 50 km, (c-d) 67.5 km, (e-f) 75 km, and (g-h) 100 km.

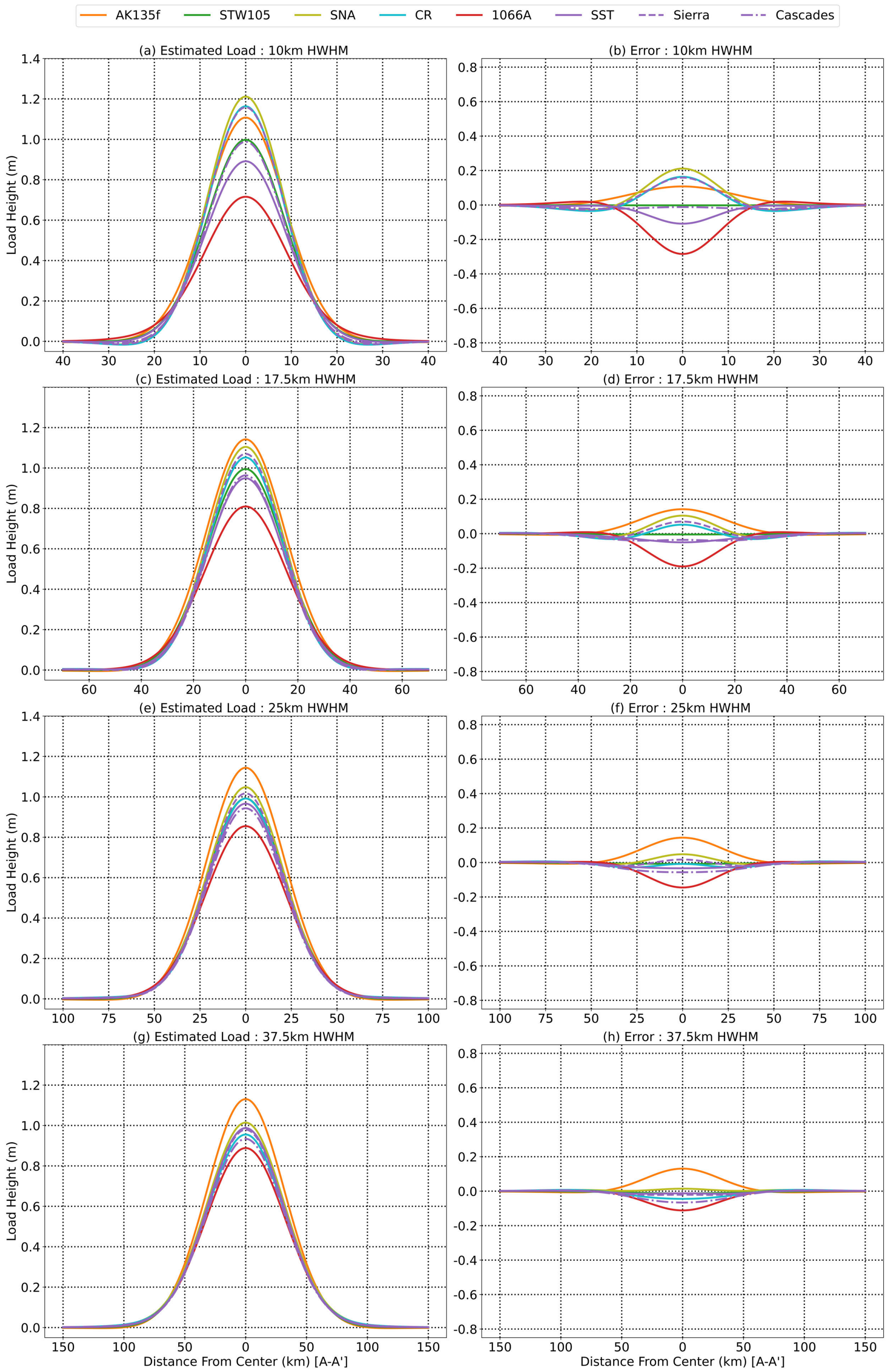

Figure S5. Estimated surface load and associated error for inversion estimates assuming the SNREI Earth structures shown in Fig. 1 along the profile A-A' in Fig. 2 for surface loads corresponding to HWHMs of: (a-b) 175 km, (c-d) 250 km, (e-f) 500 km, and (g-h) 750 km.

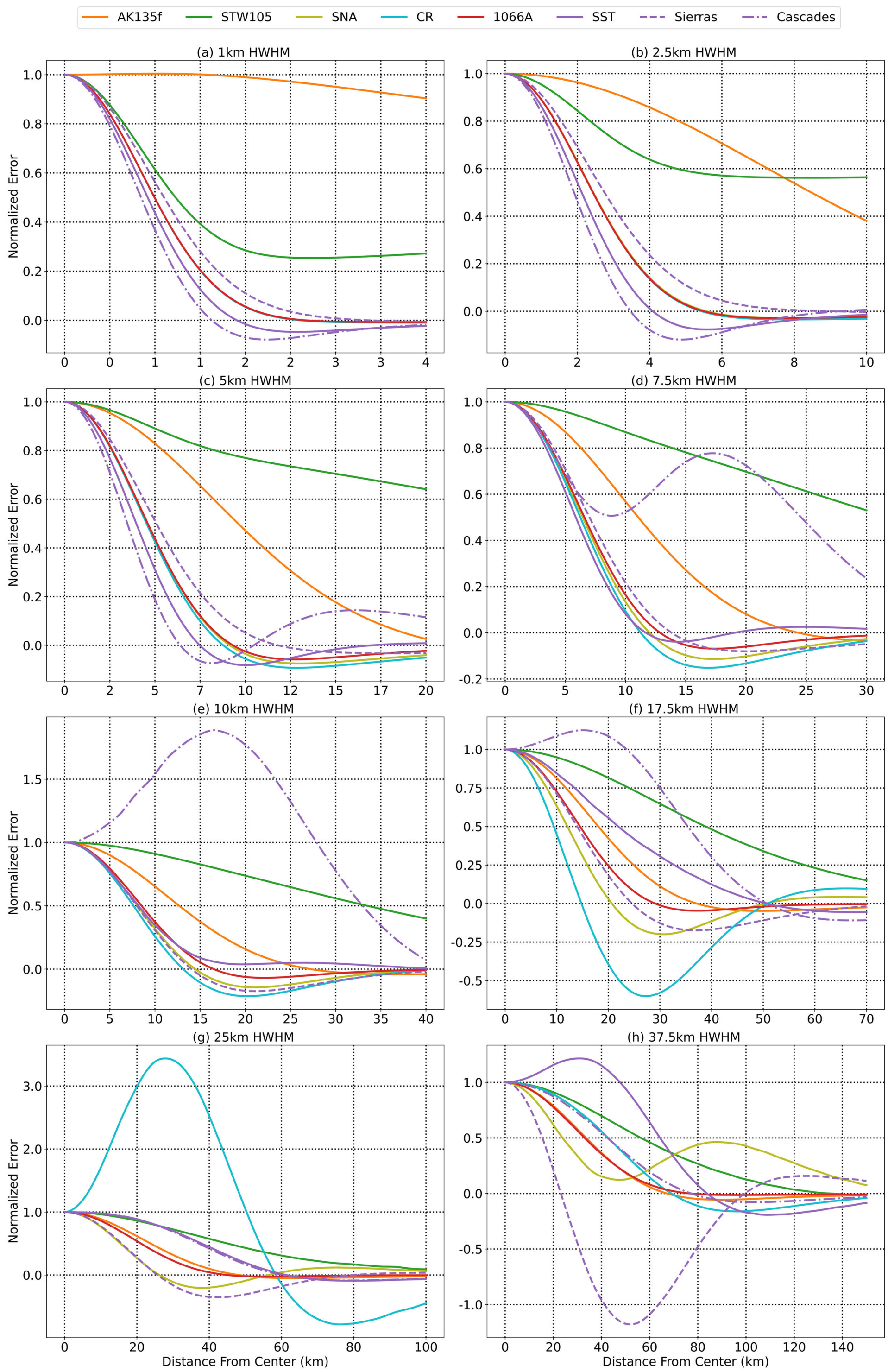

Figure S6. Error is estimated surface load normalized by the misfit at the center of the load for surface loads corresponding to HWHMs between 1 and 37.5 km.

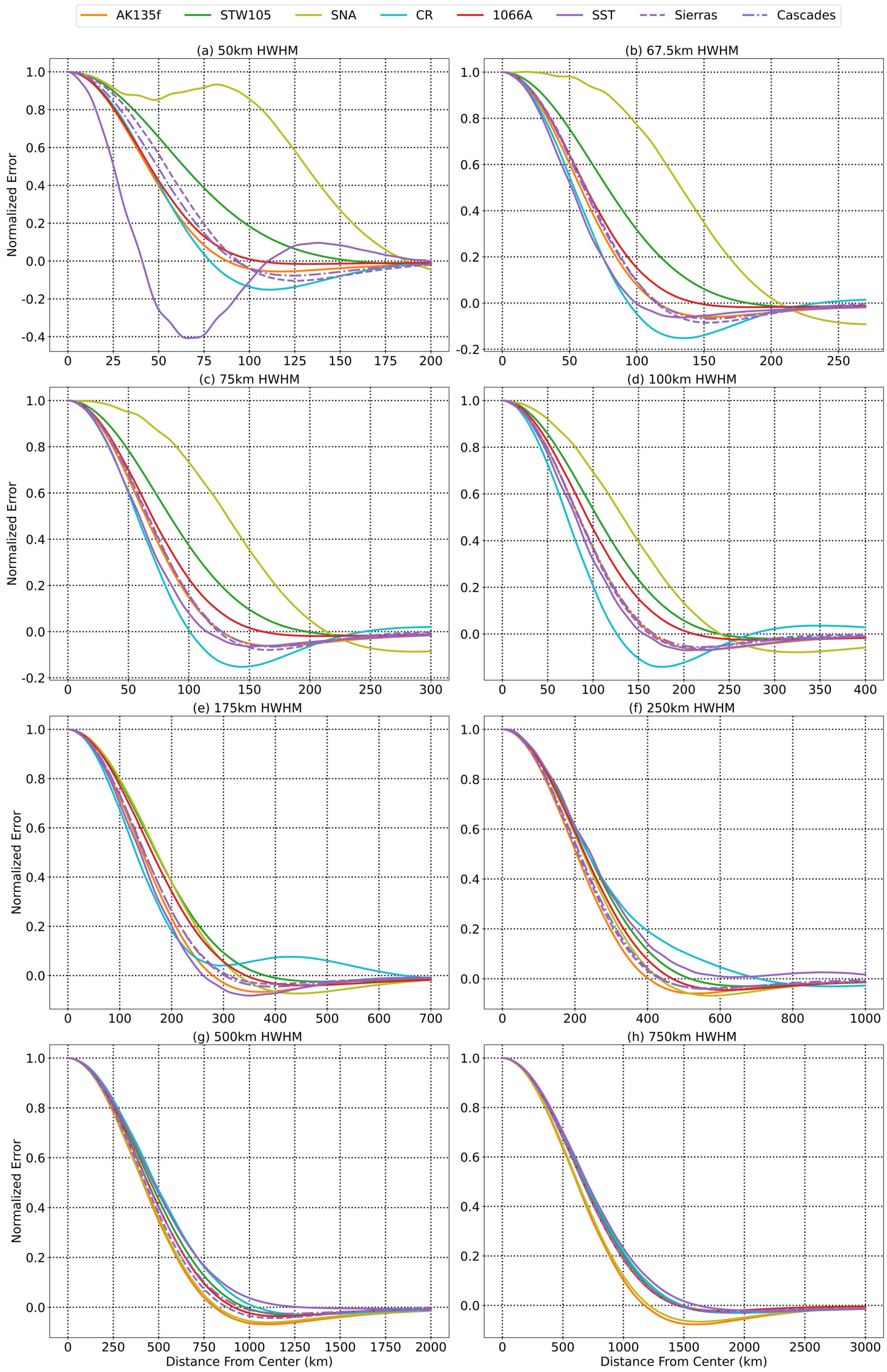

Figure S7. Error is estimated surface load normalized by the misfit at the center of the load for surface loads corresponding to HWHMs between 50 and 750 km.

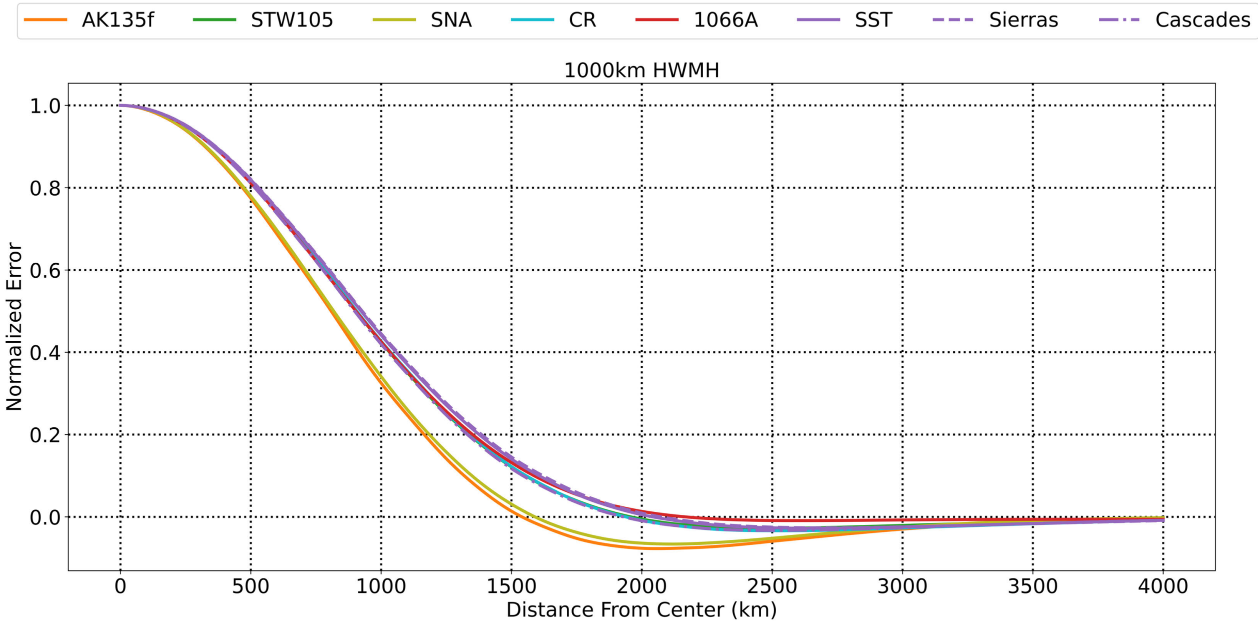

Figure S8. Error is estimated surface load normalized by the misfit at the center of the load for a surface loads with a HWHM of 1000 km.

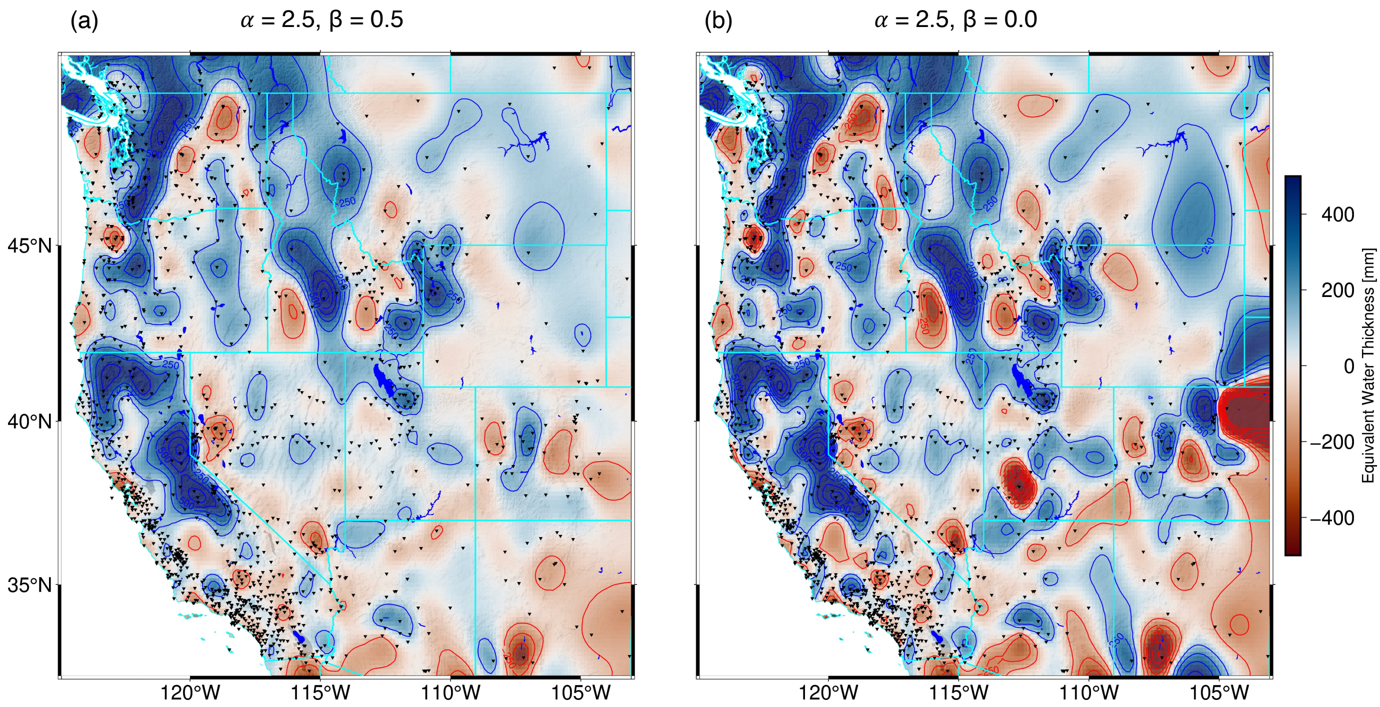

Figure S9. Estimated seasonal change in storage for the month of April 2017. (1) estimates produced using eq.2 (b) estimates produced using equation eq.1 which yield large gains/losses in the eastern portion of our model domain. Units are meter of equivalent water thickness. Contours represent 250 mm of water loss/gain.

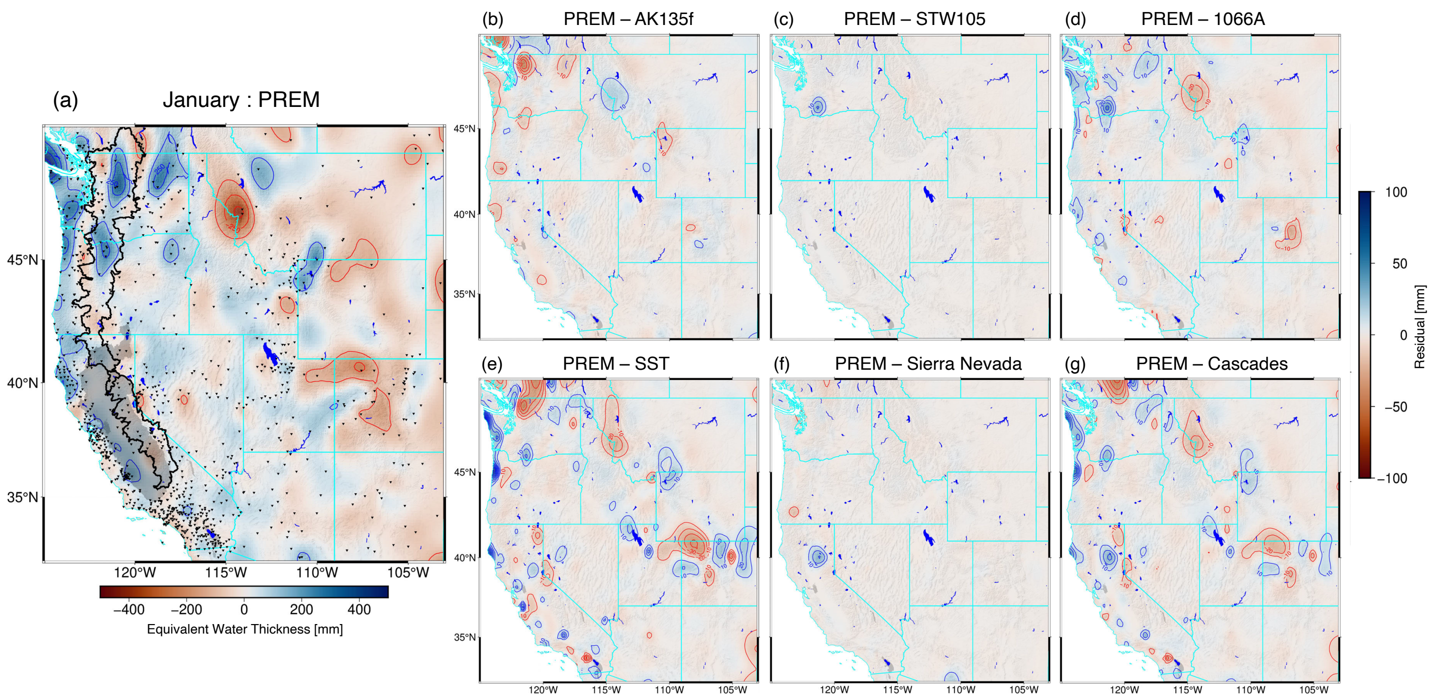

Figure S10. a) Multi-year monthly stacked estimate of seasonal change in storage for the month of January. Contours represent 125 mm intervals of equivalent water thickness. Direct differences between pairs of TWS estimates for the month of April using select Earth models: (b) PREM and AK135f, (c) PREM and STW105, (d) PREM and 1066A, (e) PREM and LITHO1.0 model for the SST River Basin, (f) PREM and LITHO1.0 model for the Sierra Nevada, and (g) PREM and LITHO1.0 model for the Cascade Range. The color bars at right denotes the amplitude of the residuals between TWS estimates. Contours represent 10 mm residual intervals of equivalent water thickness.

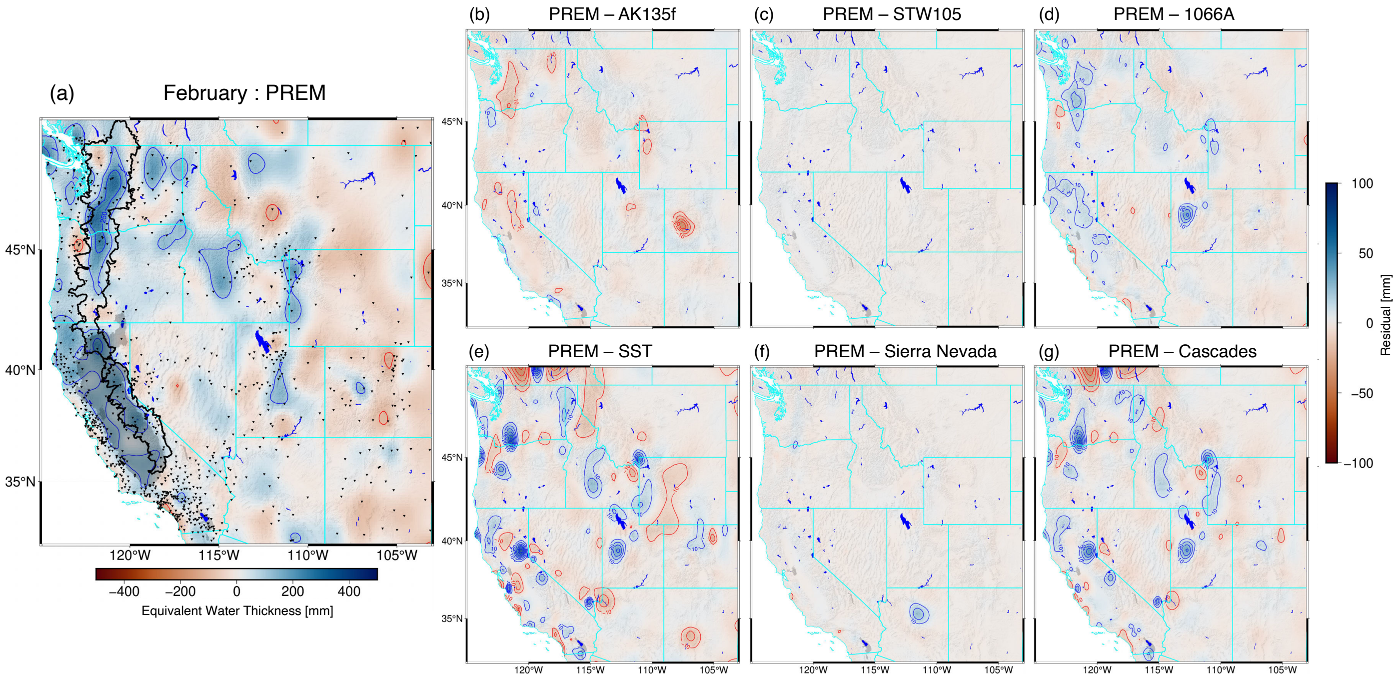

Figure S11. a) Multi-year monthly stacked estimate of seasonal change in storage for the month of February.

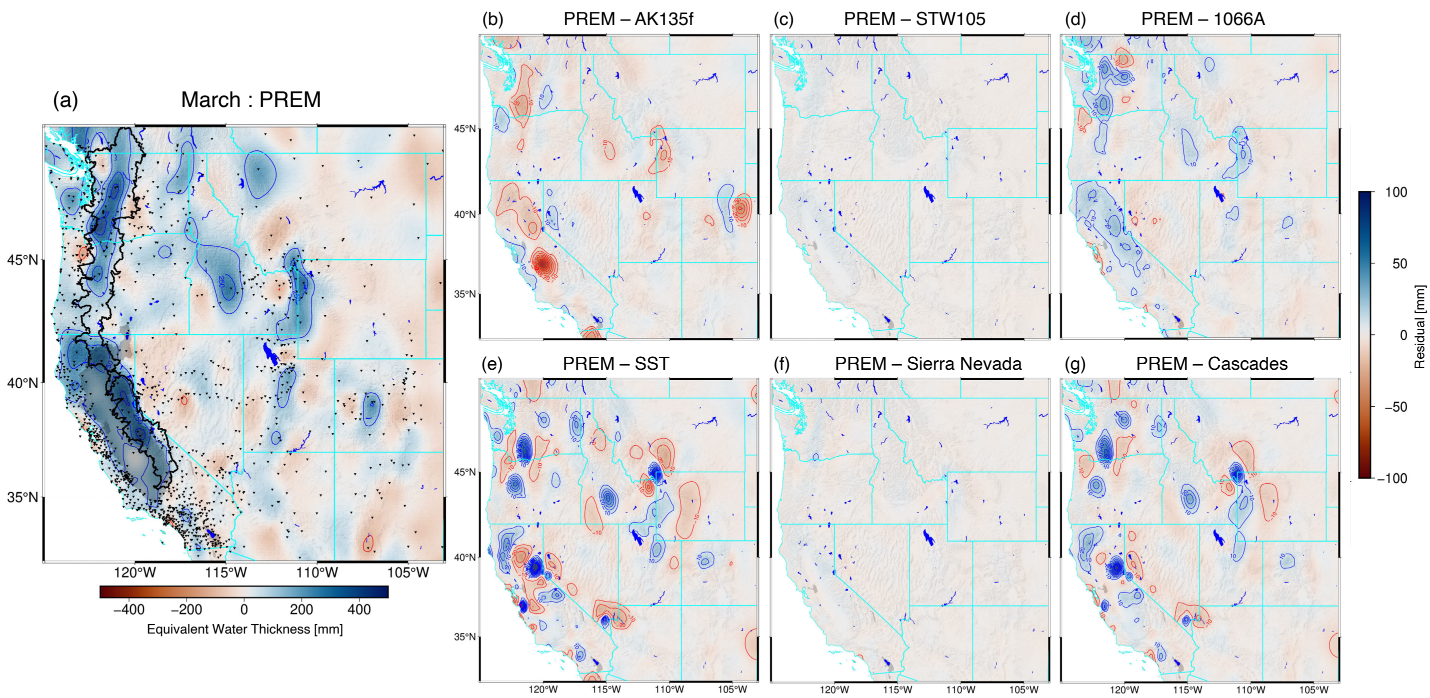

Figure S12. a) Multi-year monthly stacked estimate of seasonal change in storage for the month of March.

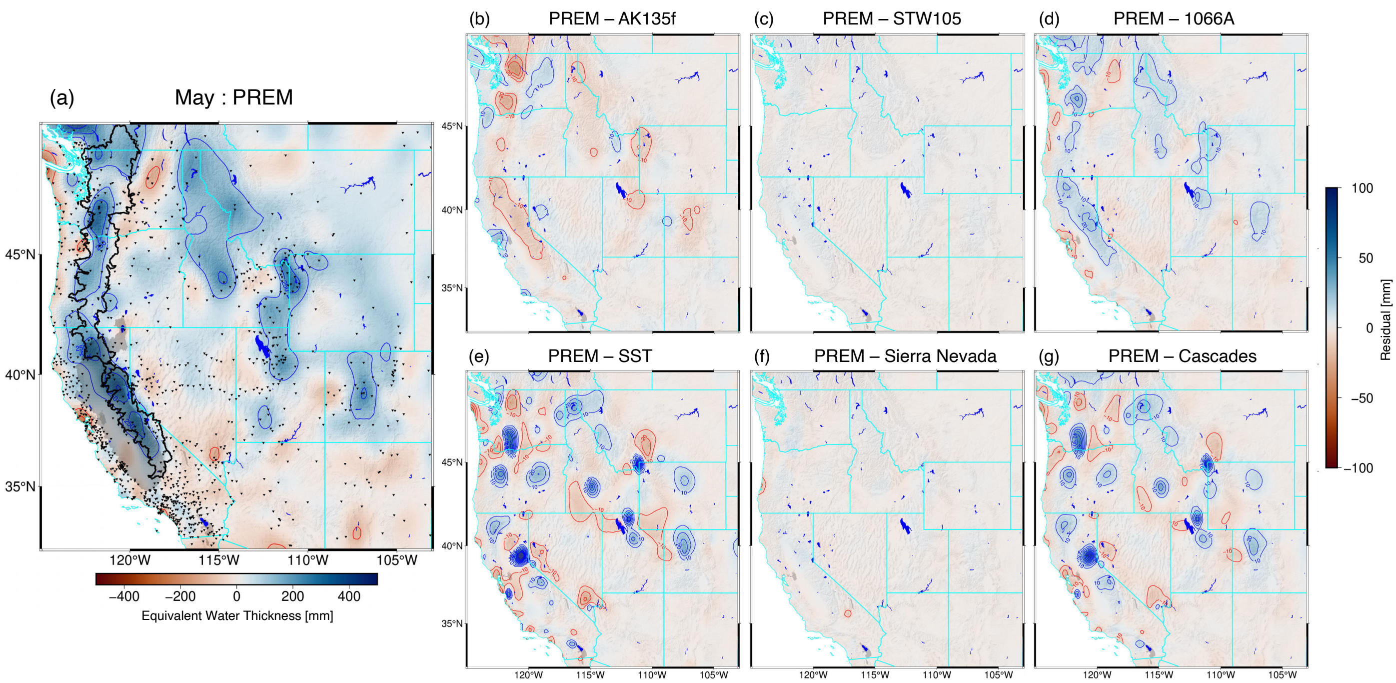

Figure S13. a) Multi-year monthly stacked estimate of seasonal change in storage for the month of May.

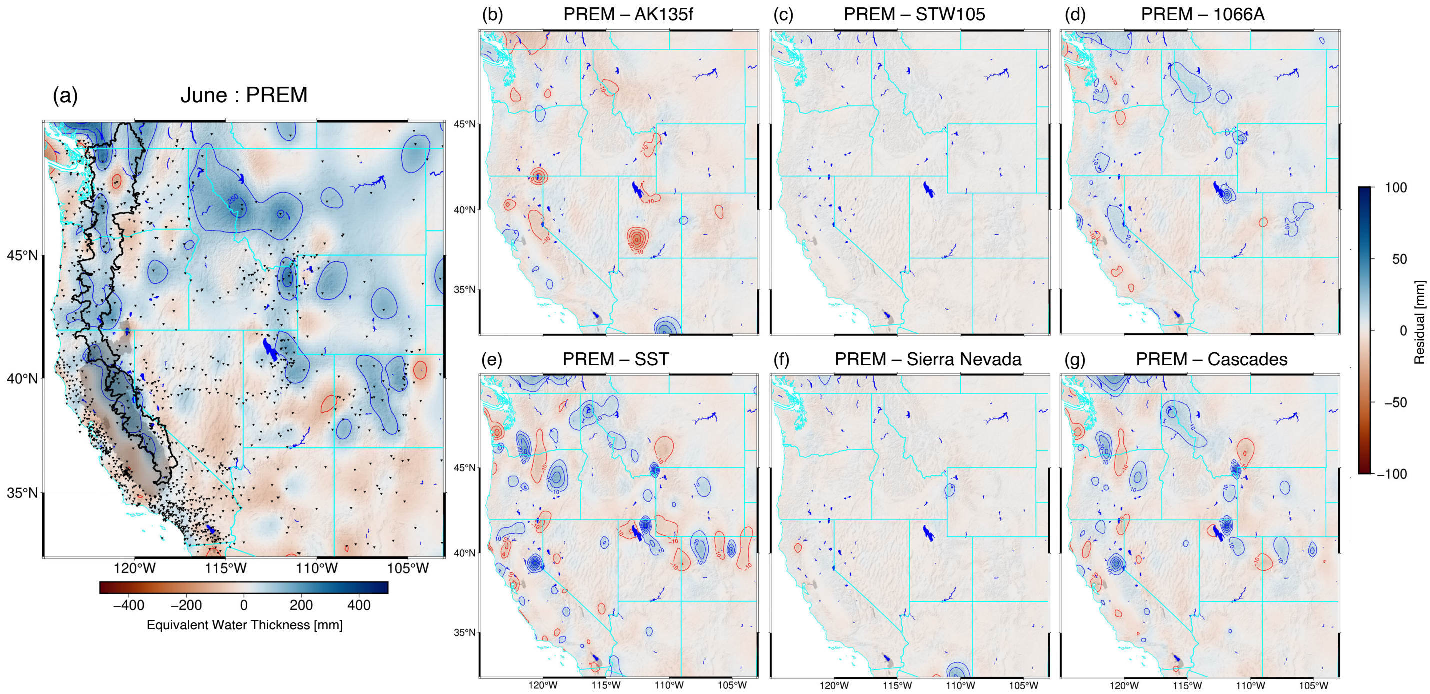

Figure S14. a) Multi-year monthly stacked estimate of seasonal change in storage for the month of June.

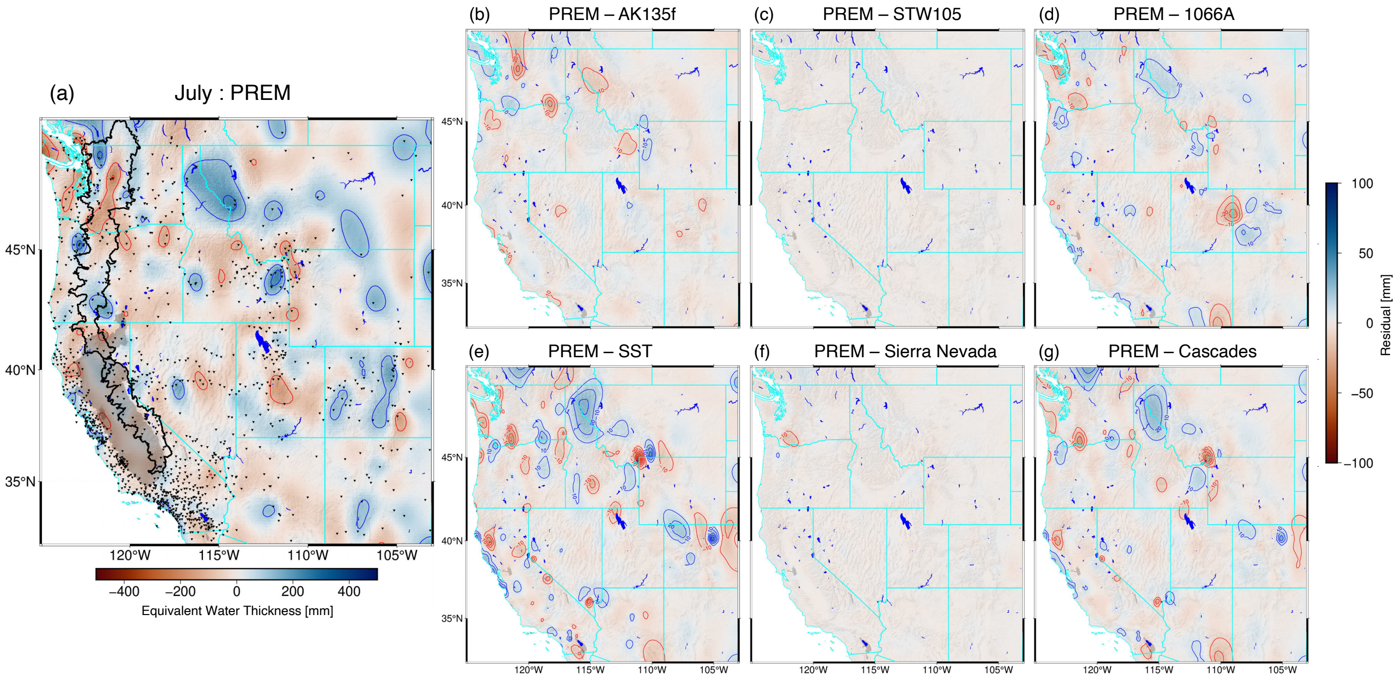

Figure S15. a) Multi-year monthly stacked estimate of seasonal change in storage for the month of July.

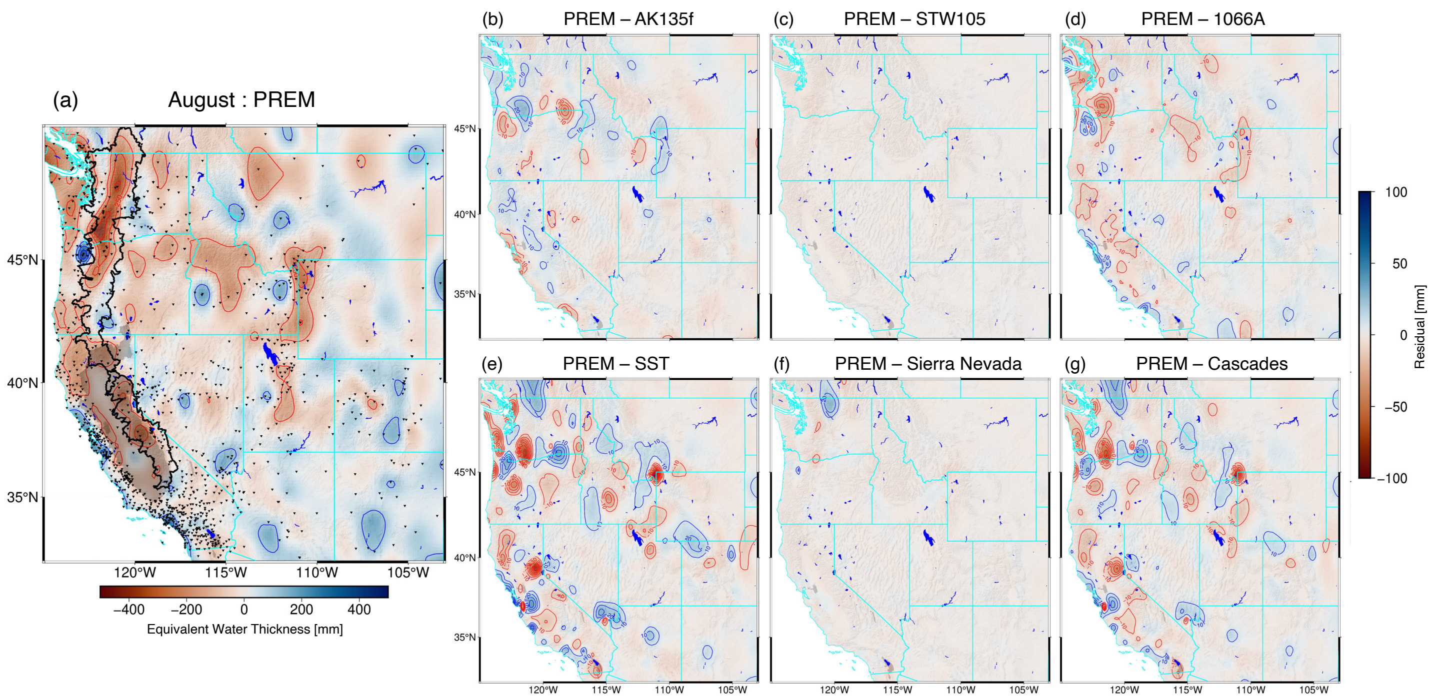

Figure S16. a) Multi-year monthly stacked estimate of seasonal change in storage for the month of August.

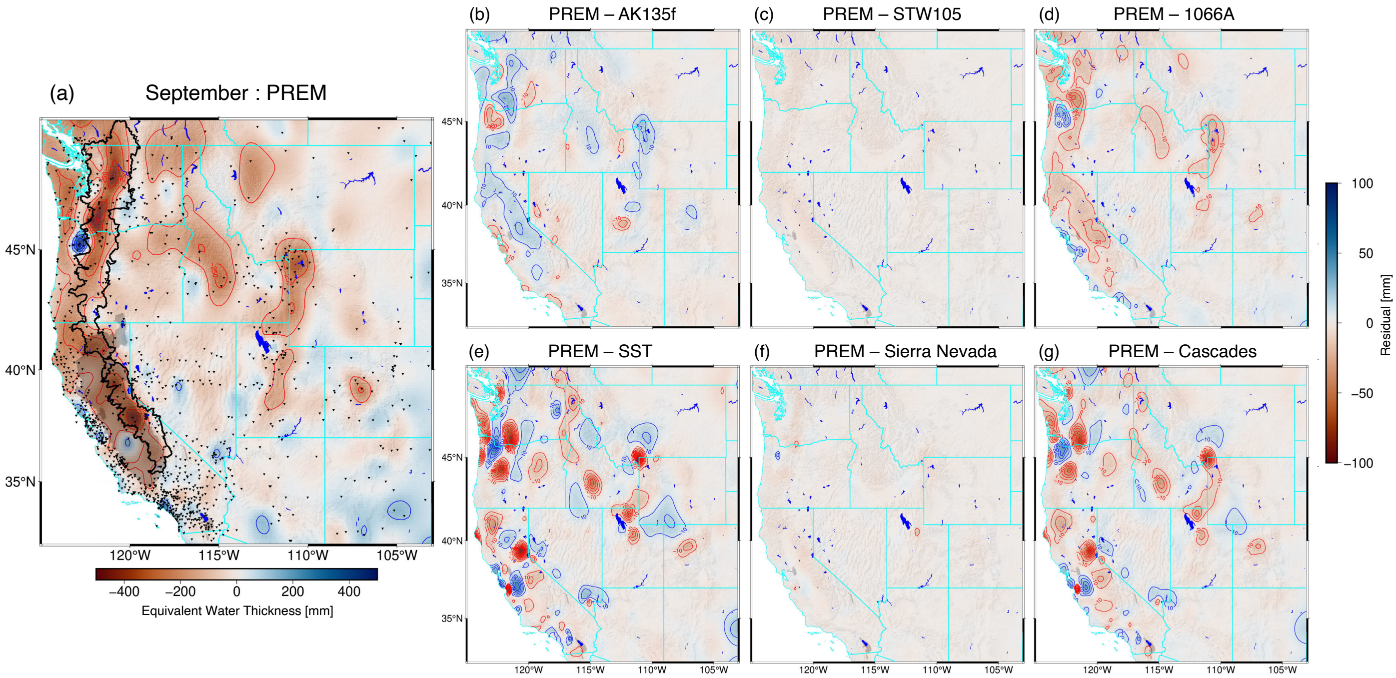

Figure S17. a) Multi-year monthly stacked estimate of seasonal change in storage for the month of September.

94

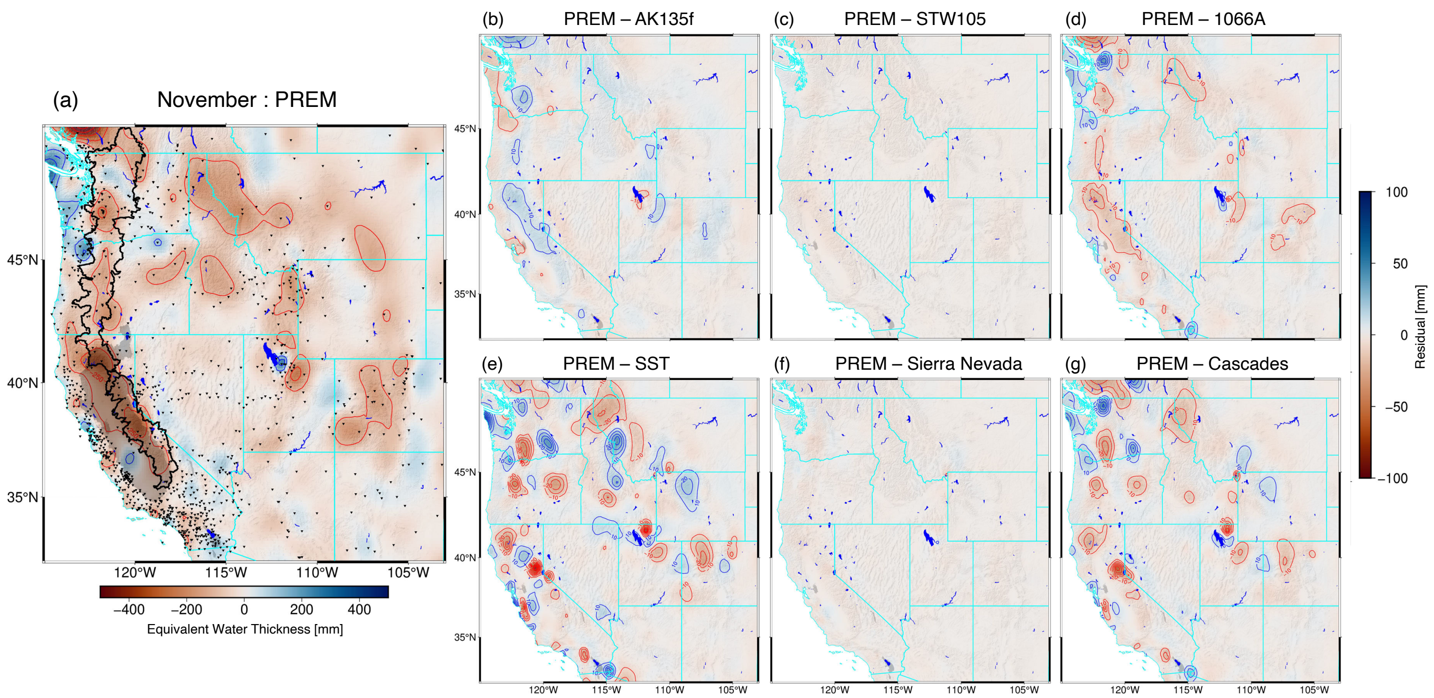

95

96 **Figure S18.** a) Multi-year monthly stacked estimate of seasonal change in storage for the month

97 of November.

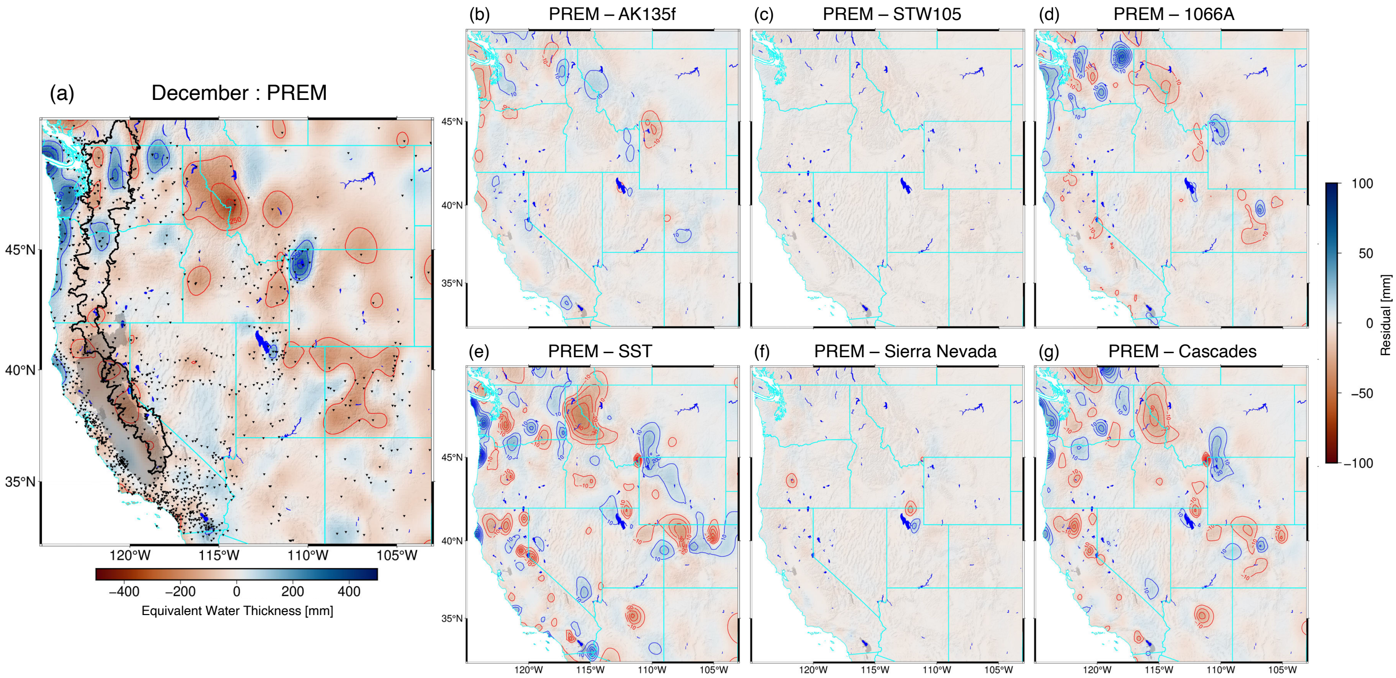

Figure S19. a) Multi-year monthly stacked estimate of seasonal change in storage for the month of December.

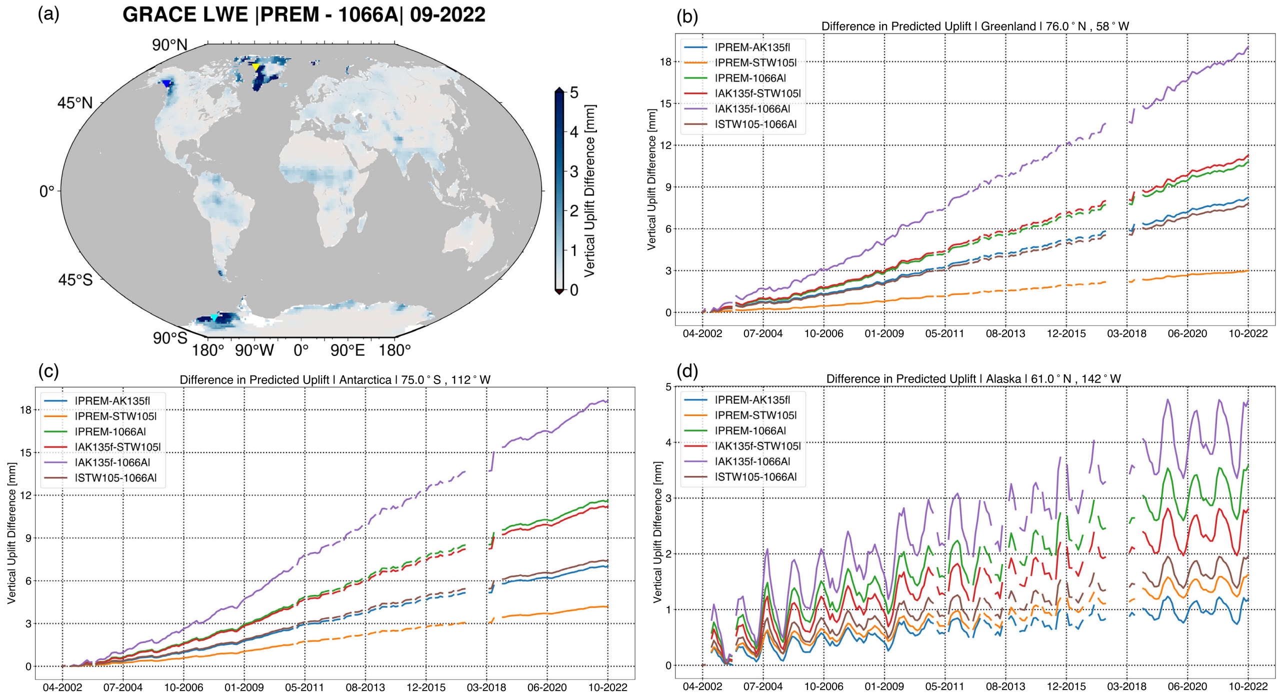

Figure S20. a) Amplitude of the difference in predicted VLM between predictions derived from PREM and 1066A for the month of September 2022. Inverted triangles represent sampling locations for the time series of VLM depicted in panels (b-d). Difference in predicted VLM between April 2002 and September 2022 for select Earth models at : (b) 76.0° N, 58° W on the western portion of the Greenland Ice Sheet, (c) 75° S, 112° W in western Antarctica, and (d) 61.0° N, 142° W in southeastern Alaska. Gaps in predicted VLM depicted here represent data gaps in the time series of GRACE and GRACE-FO.

Dataset S1. Final stations used to invert observed vertical displacements within the western U.S. to estimate seasonal changes in terrestrial water storage within the region between January 2006 and September 2022. The steps followed to determine the final set of stations used in this study are described in the main text of this manuscript.

Dataset S2. Full dataset of inversion solutions (txt format) and input surface load models used in the synthetic tests section of this work. Each file's name in the data set describes both the size of the load the solution corresponds to and the Earth model used in the design matrix of the inversion.

Dataset S3. Full dataset of inversion solutions (txt format) for seasonal TWS changes in the western U.S. between January 2006 and September 2022. Each file's name indicates the Earth model that used to construct the design matrix of the inversion.